THE JOURNAL OF PHYSICAL CHEMISTRY A

The Onset of H + Ketene Products from Vinoxy Radicals Prepared by Photodissociation of Chloroacetaldehyde at 157 nm

Chow-Shing Lam, Jonathan D. Adams, and Laurie J. Butler*

The James Franck Institute and Department of Chemistry, The University of Chicago, Chicago, Illinois 60637 United States

Supporting Information

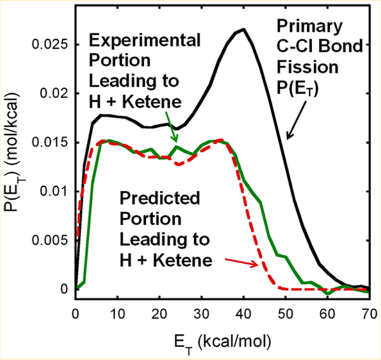

ABSTRACT: We investigate the unimolecular dissociation of the vinoxy radical (CH_2CHO) prepared with high internal energy imparted from the photodissociation of chloroacetaldehyde (CH_2ClCHO) at 157 nm. Using a velocity map imaging apparatus, we measured the speed distribution of the recoiling chlorine atoms, Cl($^2P_{3/2}$) and Cl($^2P_{1/2}$), and derived from this the resulting distribution of kinetic energy, $P(E_T)$, imparted to the Cl + vinoxy fragments upon dissociation. Using conservation of energy, the distribution of kinetic energy was used to determine the total internal energy distribution in the radical. The $P(E_T)$ derived for the C−Cl bond fission presented in this work suggests the vinoxy radicals are mostly formed in the $\tilde{A}$ state. We also took ion images at m/z = 42 and m/z = 15 to characterize the branching between the unimolecular dissociation channels of the vinoxy radical to H + ketene and methyl + CO products. Our results show a marked change in the branching ratio between the two channels from the previous study on the photodissociation of chloroacetaldehyde at 193 nm by Miller et al. (*J. Chem. Phys.*, **2004**, 121, 1830) in that the production of ketene is now favored over the production of methyl. To help analyze the data, we developed a model for the branching between the two channels that takes into account how the change in rotational energy en route to the products affects the vibrational energy available to surmount the barriers to the channels. The model predicts the portion of the C−Cl bond fission $P(E_T)$ that produces dissociative vinoxy radicals, then predicts the branching ratio between the H + ketene and CH_3 + CO product channels at each E_T. The model uses Rice−Ramsperger−Kassel−Marcus rate constants at the correct sums and densities of vibrational states while accounting for angular momentum conservation. We find that the predicted portion of the $P(E_T)$ that produces H + ketene products best fits the experimental portion (that we derive by taking advantage of conservation of momentum) if we use a barrier height for the H + ketene channel that is 4.0 ± 0.5 kcal/mol higher than the isomerization barrier en route to CH_3 + CO products. Using the G4 computed isomerization barrier of 40.6 kcal/mol, this gives an experimentally determined barrier to the H + ketene channel of 44.6 kcal/mol. From these calculations, we also predict the branching ratio between the H + ketene and methyl + CO channels to be ∼2.1:1.

I. INTRODUCTION

Vinoxy is one of the most frequently studied radicals due to its importance as an intermediate in combustion; it is a product in the reaction of O(^{3}P) with ethene[1] and propene,[2] and of OH with ethyne.[3] These reactions are commonly present in combustion of larger aliphatic[4] or aromatic[5] compounds. The vinoxy radical is also known to undergo a fast reaction with NO_2 in the atmosphere and could possibly contribute to the photochemical production of smog.[6] Another atmospheric process involving vinoxy is the ozonolysis of propene, which generates a Criegee intermediate, CH_3CHOO, that can subsequently decompose to vinoxy + OH.[7] Such reactions serve as a low-light source of OH in the atmosphere.

The unimolecular dissociation of the vinoxy radical has been of great interest for decades. Two pathways are viable. One is the fission of the C−H bond to produce H + ketene (channel 1), and the other yields CH_3 + CO via an isomerization to the acetyl radical (channel 2).

$$CH_2CHO \rightarrow CH_2CO\ (\text{ketene}) + H \tag{1}$$

$$CH_2CHO \rightarrow CH_3CO\ (\text{acetyl}) \rightarrow CH_3 + CO \tag{2}$$

To study the branching, Osborn et al.[8] prepared the radical primarily in the $\tilde{B}$ state (3.569 eV above ground state) by photodetachment of the vinoxide ion, CH_2CHO^-, generated by a discharge source. The branching between the two channels was found to be 4:1, in agreement with their Rice−Ramsperger−Kassel−Marcus (RRKM) predictions assuming internal conversion to the ground electronic state. Previous work in our group[9] on the photodissociation of methyl vinyl ether generated vinoxy radicals primarily in the $\tilde{A}$ state (0.99 eV above ground state). That study found that the branching to the CH_3 + CO products was not discernible underneath the other source of methyl radicals from the photodissociation of methyl vinyl ether. In a following study,[10] we prepared the vinoxy radical in the ground electronic state, $\tilde{X}$, by photodissociation of the precursor chloroacetaldehyde at 193 nm.

Received: February 4, 2016
Revised: March 22, 2016
Published: April 19, 2016

DOI: 10.1021/acs.jpca.6b01256

The nascent vinoxy was produced with a distribution of internal energies peaked at 40 kcal/mol, which is much lower than that in the work of Osborn et al. The results showed negligible (<2%) dissociation to H + ketene in contrast to the RRKM predicted branching based on the barrier heights calculated at the G3//B3LYP/6-31G(d) level of theory. In that paper, we suggested that nonadiabatic recrossing might be inhibiting the H + ketene product channel.

To understand the experimental results, several groups pursued theoretical calculations. Early studies focused on the mechanism for internal conversion from $\tilde{B} \rightarrow \tilde{A} \rightarrow \tilde{X}$. Matsika and Yarkony[11] applied a multireference configuration interaction method to locate accessible avoided crossings and conical intersections. They suggested that a radiationless transition between the $\tilde{B}$ and $\tilde{A}$ states occurs via a local minimum resulting from an avoided crossing, and then conversion from the $\tilde{A}$ state to the ground state occurs via a conical intersection. This mechanism provides computational support for the observations of Osborn et al., elucidating a mechanism that converts radicals in the $\tilde{B}$ state to the ground state. Following this conversion, the dissociation dynamics is then governed by the ground-state potential energy surface (PES). Their work also provides a mechanism for the formation of products in the photodissociation of methyl vinyl ether as the radicals produced in the $\tilde{A}$ state can convert to the ground state via the conical intersection and then evolve further on the ground-state PES. Since the lowest energy conical intersection is ~3000 cm^{-1} above the $\tilde{A}$ state minimum, the internal energy imparted to the radical should be enough to access this point. However, not enough internal energy was provided to the radical to access the $\tilde{B}$ state. The evolution of the excited states is further supported by the quantum dynamics study done by Piechowska-Strumik et al.; however, they could not conclude that all relaxation from the $\tilde{B}$ state to the $\tilde{A}$ state happens via the avoided crossing.[12]

There is not yet an adequate theoretical explanation for the results of the study on the photodissociation of chloroacetaldehyde at 193 nm. In particular, we find that the H + ketene product channel of the vinoxy radical is so suppressed that a negligible amount of ketene was formed, even though the calculated barriers to both channels do not differ by more than 2 kcal/mol. Later Young and Yarkony[13] investigated the topography of the conical intersections in proximity to the transition states (TSs) en route to the H + ketene products. They concluded that the conical intersection would not facilitate any nonadiabatic recrossing to suppress the H + ketene channel. Effort has also been put into refining the quality of the calculated barriers;[14] however, modeling the branching with these refined barriers still could not accurately explain the experimental result. So, a large discrepancy with the experimentally observed branching still remains.

To resolve this, we were motivated to generate vinoxy radicals by a method that would allow us to characterize the internal energy and rotational angular momentum of the radical and incorporate both in the RRKM prediction for the product branching for comparison with the experimental results. To do this, we used a methodology similar to that in the previous study, photodissociating chloroacetaldehyde, but used 157 nm light instead. After absorbing a 157 nm photon, the molecule is promoted to an excited state that is directly repulsive in the C−Cl bond. Once that bond breaks, the vinoxy radical is produced in a collision-free environment with a range of rotational and vibrational energies. Since we expect the photodissociation of chloroacetaldehyde to evolve on a repulsive PES, the angular momentum of the nascent vinoxy radicals should be well-represented by our rotational model described in McKown et al.[15] and Brynteson et al.[16] We can thus characterize the rotational energy imparted to the radical at equilibrium geometry and at each calculated transition state. The higher internal energy of the radicals in this study should give more unstable vinoxy that can undergo subsequent unimolecular dissociation to form H + ketene.

To help analyze the data, we also developed a different model for the branching between the two channels. The model takes into account how the change in rotational energy en route to the products affects the vibrational energy available to surmount the barriers. We calculate RRKM[17] rate constants with the correct sums and densities of vibrational states (accounting for the change in rotational energy from the minimum to transition state) for each channel. The rotational energy partitioned to vinoxy depends on the relative translational energy imparted to the fragments during the photodissociation of the chloroacetaldehyde precursor; the model directly incorporates this dependence. From the primary C−Cl bond fission $P(E_T)$, the model then predicts the portions of the $P(E_T)$ that produces vinoxy radicals that go on to dissociate unimolecularly to H + ketene vs methyl + CO products. We thus generate a prediction for the branching assuming the dissociation of vinoxy occurs along its ground-state PES. By taking advantage of momentum conservation in the dissociation to H + ketene, we can then directly compare the predictions of this model to the data taken. The analysis provides an independent measure of the barrier to the H + ketene channel (under the assumption that the dissociation is adiabatic and well-predicted by RRKM theory).

II. METHODS

A. Velocity Map Imaging Apparatus. The two-dimensional velocity map imaging experimental setup used in this work has been described previously,[18,19] so we provide a summary here. A 3% beam of chloroacetaldehyde (50% solution in water from Sigma-Aldrich, without further purification) was created by bubbling helium gas through the liquid sample to a total backing pressure of ~600 Torr. The beam was supersonically expanded at room temperature through a General Valve Iota One pulsed valve with an orifice diameter of 0.8 mm. After passing through a skimmer, the molecules were photodissociated using vertically polarized 157 nm light from a GAM (EX350F) F_2 excimer laser. Since atmospheric O_2 strongly absorbs 157 nm light, the excimer was fitted with a line leading to the main vacuum chamber that was constantly purged with N_2 gas. Along this line, the beam passed through a CaF_2 thin-film polarizer to obtain the desired polarization and a MgF_2 lens that focused it to approximately a 2 mm × 1 mm spot in the interaction region. The MgF_2 lens also served as the barrier between the purging line and the main vacuum chamber. Typical pulse energies were ~0.6 mJ/pulse. Approximately 40 ns after photodissociation, the products were ionized using one of two schemes discussed below.

For the detection of the Cl atom, we used 2 + 1 resonance enhanced multiphoton ionization (REMPI) to selectively ionize the $Cl(^2P_{3/2})$ and $Cl(^2P_{1/2})$ photofragments with 235.34 nm ($4p\ ^2D_{3/2} \leftarrow 3p\ ^2P_{3/2}$) and 235.20 nm ($4p\ ^2P_{1/2} \leftarrow 3p\ ^2P_{1/2}$) photons, respectively. These wavelengths were generated by tripling the output of a Lambda Physik Fl 3002 dye laser (LDS 698 dye) that was pumped by a pulsed Continuum Powerlite

Precision 9020 Nd:YAG laser. The ~706 nm dye output passed through a potassium dihydrogen phosphate (KDP) crystal, which doubled the frequency, and then the second harmonic was mixed with the fundamental in a β-barium borate crystal to produce vertically polarized photons at the REMPI wavelength. This light was separated from the other frequencies using a Pellin−Broca prism and was focused using a 25.4 cm focusing lens into the chamber, where it crossed the molecular beam at a right angle. The accumulated signal was obtained by then scanning over a Doppler profile of ±0.008 nm from the line center.

For the detection of ketene and methyl radical products, we used 10.5 eV photoionization generated by tripling the 355 nm output of a pulsed Continuum Surelite I-20 Nd:YAG laser. The 355 nm beam passed through a beam expander (focal length = −150 mm and focal length = 300 mm at 588 nm) and then through two lenses that focused the light into a 21 cm low-pressure gas cell filled with 24 Torr of high-purity Xe (>99.995%). The gas cell was mounted onto the main vacuum chamber with a MgF_2 lens (focal length = 120.3 mm at 193 nm) that served as the barrier between the cell and the chamber. The lens recollimated the 355 nm light while focusing the 118 nm light.

Following photodissociation and photoionization, the electrostatic lens optics with repeller and extractor voltages in a 1.404:1 ratio (3932 and 2800 V, respectively) accelerated the spherically expanding ions down an ~557 mm grounded time-of-flight tube toward the detector. The Burle3040FM detector is comprised of a position-sensitive Chevron microchannel plate (MCP) assembly coupled to a P20 phosphor screen. The front plate of the MCP was pulsed at −750 V for 80 ns to selectively detect ions based on their arrival time. The voltage of the phosphor screen was maintained at 3.3 kV above the potential at the rear plate of the MCP. Ions colliding with the MCP produce an electron cascade, which induces phosphorescence on the screen in the position the ion struck. A cooled charged-coupled device camera (La Vision Imager 3QE) with a standard 35 mm lens was used to take images. The images were then processed using Houston's ion counting[20] method; speed distributions, along with angular distributions, were obtained using the BASEX code of Dribinski et al.[21] The timing for the opening of the pulsed valve, firing the lasers, pulsing the MCP, and capturing the ion images was controlled by a digital delay generator (Stanford Research DG535) with a repetition rate of 20 Hz.

B. Computational Method. We calculated minima and transition states relevant to the dissociation of ground-state vinoxy radicals, updating our previous calculations at the G3//B3LYP level of theory with the more recent G4 protocol. Optimized molecular geometries and vibrational frequencies were found using the B3LYP density functional and the 6-311++G(3df,2p) basis set. The geometries converged to a root-mean-square (rms) force below 1×10^{-5} and an rms displacement below 4×10^{-5}, where both values are in atomic units. Wave functions for doublet species were spin-unrestricted, and wave functions for singlet species were spin-restricted. The computation of the zero-point vibrational energies used the B3LYP/6-311++G(3df,2p) vibrational frequencies scaled by 0.9854[22] as the G4 method required.[23] The G4 method is the latest in the series of Gn theories, which are composite methods based on a sequence of single-point energy calculations. To utilize our model and calculate the portion of the $P(E_T)$ that leads to a particular channel, we also ran an intrinsic reaction coordinate (IRC) calculation at the B3LYP/6-311++G(3df,2p) level. The calculations use the Gaussian 09 program, version A.02.[24]

III. RESULTS

In the following paragraphs, we present the velocity map imaging data for the photodissociation of chloroacetaldehyde and the subsequent dissociation of the vinoxy radical along with the calculations that allow us to predict the portion of the primary C−Cl bond fission $P(E_T)$ that gives vinoxy radicals that dissociate via a particular channel. We begin with a brief review of the PES for the unimolecular dissociation channels of the vinoxy radical. Section IIIB details the center-of-mass translational energy distributions obtained from the detection of the chlorine atom cofragment of vinoxy from the primary photodissociation. Section IIIC describes the detection of ketene and identifies its source by examining its kinetic energy distribution. Section IIID details the model used to predict the branching between the H + ketene and methyl + CO channels. In Section IIIE, we present the results of the calculations predicting the portion of the primary $P(E_T)$ that leads to vinoxy radicals that dissociate to H + ketene and methyl + CO products. The results evidenced a marked change in the product branching from the previous study that generated vinoxy radicals from the photodissociation of chloroacetaldehyde at 193 nm. The CH_3 + CO channel dominates the branching near the threshold, while the H + ketene channel dominates at higher vibrational energies where the branching fractions level out. In Section IIIF, we present the data recorded at m/z = 15; the contributions to this signal include the dissociation of vinoxy to CH_3 + CO and the dissociative ionization of stable vinoxy radicals to CH_3^+ + CO.

A. Electronic Structure Calculations. To characterize the rotational and vibrational energy distribution of the vinoxy radicals formed by photolysis, the molecular conformers of the precursor chloroacetaldehyde must be considered. On the basis of our calculations, there are three conformers of chloroacetdaldehyde: one syn conformer and two anti conformers, which differ in their respective Cl−C−C−O dihedral angles (see Supporting Information). The zero-point level of the syn conformer in the gas phase is slightly higher than the anti conformers due to the unfavorable interaction between the Cl atom and the O atom. Their single-point energies were calculated at 0 and 298 K, the nozzle temperature. Accounting for the degeneracy of the anti structures, the relative populations are summarized in Table 1. The PES for the unimolecular dissociation of the vinoxy radical has been revisited at the G4//B3LYP/6-311++G(3df,2p) level of theory. Using the zero-point levels of the optimized structures, we report the recalculated energy barriers along each secondary dissociation pathway. Unsurprisingly, the difference between

Table 1. Relative Energy, Percent Composition in the Molecular Beam, C−Cl Bond Dissociation Energy, and Average Internal Energy of the Conformers of Chloroacetaldehyde at 25°C

conformer	relative energy[a] (kcal/mol)	percentage in molecular beam	D_o(C−Cl) (kcal/mol)	average internal energy (kcal/mol)
anti	0	92.68%	73.4	1.20
syn	1.09	7.32%	72.3	1.08

[a] The relative energies are with respect to the anti conformer.

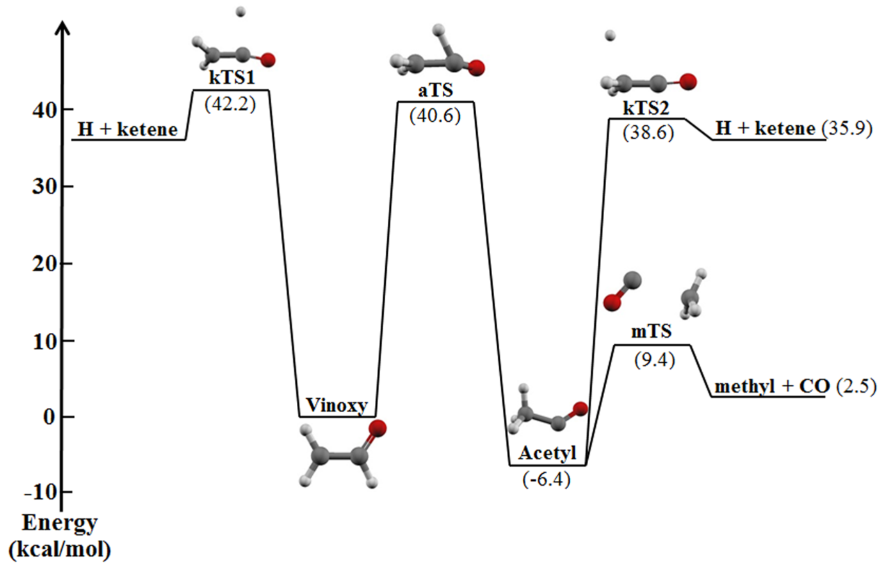

Figure 1. Selected minima and transition states on the PES for unimolecular dissociation of the vinoxy radical. The energies of the stationary points relative to the zero-point level of ground-state vinoxy are given in parentheses. They are calculated at the G4//B3LYP/6-311++G(3df,2p) level of theory and include harmonic zero-point energy corrections.

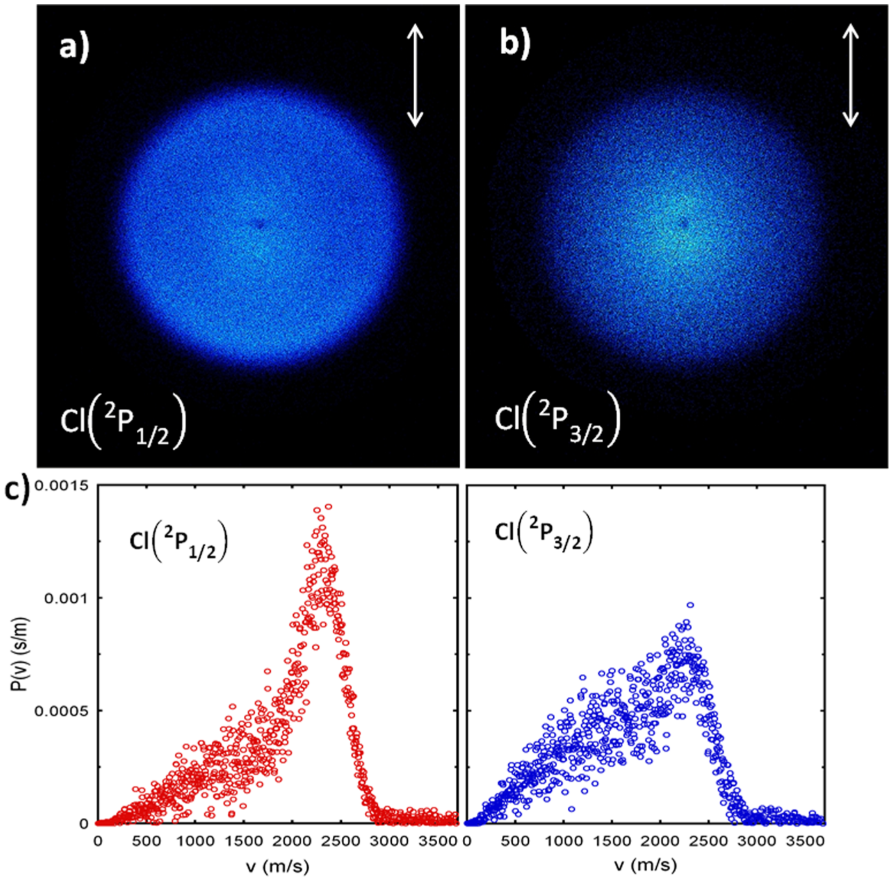

Figure 2. Background-subtracted images for (a) $Cl(^2P_{1/2})$ and (b) $Cl(^2P_{3/2})$. The dimensions of the images shown are 928 pixels ×1040 pixels. The direction of photodissociation laser polarization is shown by the arrow in the upper right of each image. The lower frame (c) shows the corresponding speed distributions for $Cl(^2P_{1/2})$ (in red) and $Cl(^2P_{3/2})$ (in blue) normalized to unit area.

these results and our previous G3//B3LYP is very small. The computational studies by Bennett et al. and the Yarkony group have shown that the barrier heights of channel (1) and (2) should be within 2−3 kcal/mol. Nevertheless, for clarity we depict all the stationary points and transition states identified and their zero point-corrected G4 energies relative to ground-state vinoxy in Figure 1.

B. Primary Photodissociation Channels, C−Cl Bond Photofission. The goal of the study is to prepare vinoxy radicals with a vibrational energy distribution spanning the barriers en route to both dissociation channels. Our velocity map imaging apparatus enables us to characterize the speed and angular distributions of the fragments resulting from photodissociation of the halogenated precursor. Here, we report the measured speed of the recoiling chlorine atoms and derive from this the resulting distribution of kinetic energy imparted to the Cl + vinoxy fragments upon dissociation. The recoiling chlorine atoms from the photolytic cleavage of C−Cl bond in the precursor may be formed in either of two spin−orbit states, $^2P_{3/2}$ or $^2P_{1/2}$. Using REMPI, we selectively ionize and detect the recoiling chlorine atoms in their respective spin−orbit states. This C−Cl photofission translational energy distribution, $P(E_T)$, is then used to determine the internal energy distribution of the nascent vinoxy radicals.

Figure 2a,b shows the ion images of Cl($^2P_{1/2}$) and Cl($^2P_{3/2}$), respectively. These images are background-subtracted and thus show the signal from photodissociation at 157 nm and REMPI photoionization. The arrow indicates the direction of the polarization of the photolysis laser. Comparatively, the image of Cl($^2P_{1/2}$) has more counts at the outer rim. Nevertheless, both images do not give a sharp ring structure at their edges as typically observed when detecting the halogen atoms from photolysis of alkyl halides. Neither of the images display a distinctive anisotropy. Though both images are two-dimensional, by using the inverse Abel transformation in the BASEX program, they are readily reconstructed as three-dimensional scattering distributions. By integrating all solid angles at each speed, the speed distribution $P(v)$ for Cl atoms produced in each spin−orbit state can be obtained; they are shown in Figure 2c (Cl($^2P_{1/2}$) in red and Cl($^2P_{3/2}$) in blue).

The speed-dependent anisotropy parameter $\beta(v)$ is shown in the Supporting Information; it is obtained by fitting the angular distributions to $I(\theta) \propto 1 + \beta_2 P_2(\cos\theta) + \beta_4 P_4(\cos\theta)$, where P_n is the nth order Legendre polynomial, and θ is the angle between the recoil velocity vector and the electric vector of the photolysis laser. The β_4 parameter is found to be negligible for Cl atoms in each spin−orbit state; we therefore approximate the angular distribution to be $I(\theta) \propto 1 + \beta P_2(\cos\theta)$, where the anisotropy parameter, β, ranges from −1 to 2 (with $\beta = -1$ corresponding to a perpendicular transition and $\beta = 2$ corresponding to a parallel transition). The resulting values of β show that both images are not entirely isotropic. For both spin−orbit states of Cl, the value of β gradually increases from zero to ~0.5 as the recoil speed ranges from 2000 to 2500 m/s.

Relative translational energy distributions, $P(E_T)$, for Cl($^2P_{3/2}$) + CH_2CHO and Cl($^2P_{1/2}$) + CH_2CHO were calculated from the measured Cl speed distributions using momentum conservation and applying Jacobian corrections. The C−Cl fission $P(E_T)$s to form Cl($^2P_{3/2}$) and Cl($^2P_{1/2}$) are weighted by the spin−orbit branching ratio and summed together to yield the total $P(E_T)$ for all dissociation events. We determine the spin−orbit branching ratio using the expression shown in eq 3.

$$\frac{N[\mathrm{Cl}(^2\mathrm{P}_{1/2})]}{N[\mathrm{Cl}(^2\mathrm{P}_{3/2})]} = k\frac{S[\mathrm{Cl}(^2\mathrm{P}_{1/2})]}{S[\mathrm{Cl}(^2\mathrm{P}_{3/2})]} \qquad (3)$$

Here, $S[\mathrm{Cl}(^2\mathrm{P}_{1/2})]/S[\mathrm{Cl}(^2\mathrm{P}_{3/2})]$ is the ratio of the integrated signal intensity of the spin−orbit states, determined by accumulating chlorine signal while scanning over the Doppler profile of each state. By scaling with the REMPI line strength, $k = 0.85 \pm 0.10$,[25] the resulting branching ratio $N[\mathrm{Cl}(^2\mathrm{P}_{1/2})]/N[\mathrm{Cl}(^2\mathrm{P}_{3/2})]$ is calculated to be 0.82 ± 0.16. If we divide the C−Cl $P(E_T)$ into a fast component peaking near 40 kcal/mol and a broad slow component, we calculate the Cl($^2P_{1/2}$)/Cl($^2P_{3/2}$) ratio to be near unity for the fast component, and near a statistical ratio of 1:2 for the portion of the slow component with E_T less than 20 kcal/mol. The weighted $P(E_T)$s for photodissociation events leading to Cl($^2P_{3/2}$) and Cl($^2P_{1/2}$) are shown in blue and red lines, respectively, in Figure 3. Both distributions peak at 40 kcal/mol, although the distribution for Cl($^2P_{1/2}$) shows a sharper peak at this translational energy. Our total translational distribution, shown in black line in Figure 3, also peaks at ~40 kcal/mol and has an average translational energy, $\langle E_T \rangle$, of 28.5 kcal/mol. Figure 4 shows a smoothed C−Cl bond fission $P(E_T)$ generated from the $P(E_T)$ in Figure 3 by averaging the $P(E_T)$ values in each E_T range of 2.5 kcal/mol, putting the average value in the weighted center of the range. These $P(E_T)$ values are then interpolated to an even spacing in E_T.

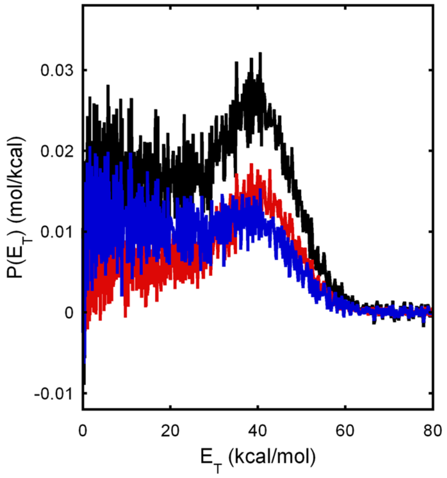

Figure 3. Total relative translational energy distribution, $P(E_T)$, for all C−Cl photofission events. The figure shows the total relative translational energy distribution (black), which is the sum of the contributions of the vinoxy + Cl($^2P_{3/2}$) $P(E_T)$ (blue) and the vinoxy + Cl($^2P_{1/2}$) $P(E_T)$ (red) derived from the imaging data in Figure 2 by applying conservation of momentum and Jacobian corrections.

The $P(E_T)$ derived from the detection of Cl also allows us to determine the internal energy distribution of all the nascent vinoxy radicals. Conservation of energy requires that the sum of the energy of the photon, $h\nu$, and the internal energy of the parent molecule prior to dissociation, E_{int}(precursor), must be equal to the energy partitioned into the product fragments. Some of this energy is consumed in breaking the C−Cl bond, D_o(C−Cl), and the remaining energy is distributed among recoil translational energy in the center-of-mass reference frame, E_T, and internal energy of the fragments, E_{int}(Cl) and E_{int}(radical)

$$\begin{aligned} &h\nu + E_{\mathrm{int}}(\mathrm{precursor}) \\ &\quad = D_o(\mathrm{C{-}Cl}) + E_T + E_{\mathrm{int}}(\mathrm{Cl}) + E_{\mathrm{int}}(\mathrm{radical}) \end{aligned} \qquad (4)$$

Using this equation, the total primary $P(E_T)$ can be used to derive the distribution of internal energy in the vinoxy radical, $P(E_{\mathrm{int}})$. The internal energy scale depicted by the upper axis in Figure 4 was calculated for C−Cl photodissociation events that produce Cl($^2P_{3/2}$). Any events producing Cl($^2P_{1/2}$) would produce vinoxy radicals with 2.5 kcal/mol less in internal energy. (In our later calculations, we explicitly determine the

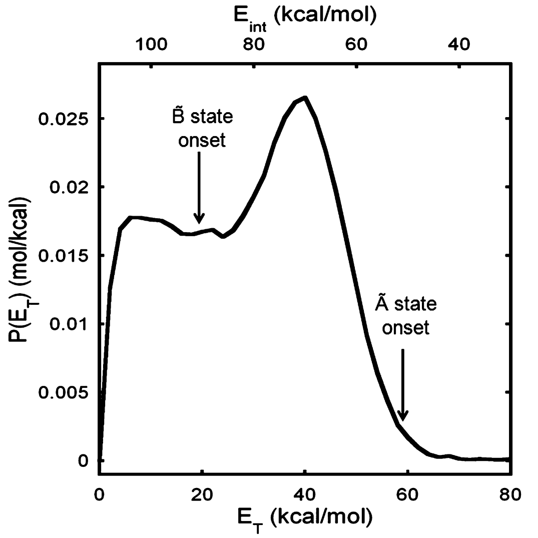

Figure 4. Total $P(E_T)$ for all C−Cl photodissociation events smoothed and interpolated from the black curve in Figure 3. The lower axis, E_T, is the translational energy imparted to the vinoxy and Cl products of the dissociation of chloroacetaldehyde; the upper axis, E_{int}, is the internal energy of the vinoxy radicals assuming they are formed in the ground electronic state and the Cl atoms are formed in the ground spin−orbit state ($^2P_{3/2}$). The labels on the plot indicate the onsets of Ã state and B̃ state vinoxy calculated by determining the maximum E_T value that would allow for either state to be formed from C−Cl photodissociation by conservation of energy. The rotational energy used in calculating the onsets was approximated using our model with the geometry of the anti conformer of the precursor and equilibrium geometry of each excited state.

internal energy distribution of vinoxy radicals produced in coincidence with both Cl($^2P_{3/2}$) and Cl($^2P_{1/2}$) as we measured the $P(E_T)$s individually.) The internal energy of the vinoxy radicals ranges from 40 to 110 kcal/mol and peaks at ∼70 kcal/mol. Since the previous study at 193 nm had a smaller range of internal energies in the radical and peaked at 40 kcal/mol, the vinoxy radicals produced in this study have more energy at their disposal for subsequent dissociation. However, we must now account for conservation of angular momentum; energy in vibrations is responsible for traversing barriers along the PES, and the internal energy in the radical is comprised of vibrational and rotational energy. Using our model below, we can approximate the rotational energy at the vinoxy equilibrium geometry and each transition state (TS), allowing us to correctly calculate the sums and densities of states for the RRKM predictions of the product branching (see Section IIID).

It is also worth investigating the possibility that C−Cl photodissociation produces vinoxy in an excited state as opposed to the ground electronic state. Using eq 4, we can calculate the relative translational energy that would correspond to the production of vinoxy radicals in either the Ã or B̃ state with zero vibrational energy (while conserving angular momentum) and Cl($^2P_{3/2}$) as the cofragment. We used our rotational model to approximate the rotational energy in terms of E_T for the vinoxy radical at its equilibrium geometry for either the Ã or B̃ state and subtract this from E_{int} of the radical. These "onsets" of excited-state vinoxy are shown in Figure 4 by arrows pointing to the E_T values with labels above describing the excited state to which they refer. The onset of the Ã state is E_T = 58.5 kcal/mol, and the onset of the B̃ state is E_T = 19.0 kcal/mol, which seem to fit well with the features of the distribution. Since the model requires a precursor geometry to calculate an angular momentum vector, the choice of the precursor to be used is important (see Section IIID) and it should be noted that the anti conformer of chloroacetaldehyde was used in the calculated onsets in Figure 4. The onsets calculated using the less probable syn conformer are 54.4 kcal/mol for the Ã state and 18.1 kcal/mol for the B̃ state. One can see that C−Cl photofission at 157 nm may produce vinoxy radicals in the Ã and B̃ states; almost the entire primary $P(E_T)$ can be attributed to vinoxy radicals in excited states based on these calculations. Our RRKM predictions proceed under the assumption that they undergo internal conversion and dissociate on the ground-state PES.

Ideally, we would also detect stable vinoxy radicals at m/z = 43 to further characterize the primary C−Cl bond fission channel, as enough energy is portioned to rotational energy to form some vinoxy radicals stable to subsequent dissociation. While the ionization energy of vinoxy is calculated to be ∼9.13 eV,[26] the significant difference in equilibrium geometry between the radical and its cation allows for little Franck−Condon overlap in the vertical region on the cationic PES. This makes detecting vinoxy at its cation mass following photoionization difficult; no photoionization spectrum for vinoxy radical at m/z = 43 has been reported in the literature. Thus, we did not attempt to accumulate data at m/z = 43. However, vinoxy radicals are found to give signal at m/z = 15 from dissociative ionization when the photon energy is above 10.3 eV.[27,28] When analyzing the signal detected at m/z = 15 in Section IIIF, we will consider possible contribution from stable vinoxy to the signal at m/z = 15.

Another primary photodissociation channel of chloroacetaldehyde is HCl elimination, which produces ketene and can thus contribute signal to the m/z = 42 data. Ideally, we would also characterize this primary channel and subtract its contribution to the m/z = 42 data leaving us with the ketene produced solely from secondary dissociation of vinoxy. However, based on the data taken at m/z = 42 and the subsequent calculations predicting the portion of the primary $P(E_T)$ leading to vinoxy that dissociates to H + ketene products, the primary HCl photoelimination channel appears to be relatively insignificant.

C. Detection of Ketene, CH_2CO. We detected the ketene product from the unimolecular dissociation of vinoxy to characterize the branching to this product channel as a function of internal energy (rotational and vibrational) in the vinoxy radical. On the same apparatus, instead of the REMPI detection scheme used to detect Cl, we employ photoionization at 10.5 eV to detect ketene. With the photon energy substantially higher than the photoionization threshold (9.62 eV[29]) but yet below the first appearance energy yielding daughter ions, (11.75 eV[29]), neutral ketene products with various recoil kinetic energies should be detected without bias. The net speed distribution derived from the ion image recorded at m/z = 42 is shown in Figure 5. The net speed, v_{net}, is the magnitude of the net velocity vector, which is the vector sum of the velocity of the vinoxy cofragment imparted during C−Cl bond fission and the velocity imparted during secondary dissociation.

The measured net speed distribution of the ketene products allows us to determine the speed distribution of the nascent vinoxy radicals that dissociate to H + ketene. Because of the overwhelming mass difference between the H + ketene cofragments, the H atom is imparted with the majority of the relative velocity vector by conservation of momentum. In other

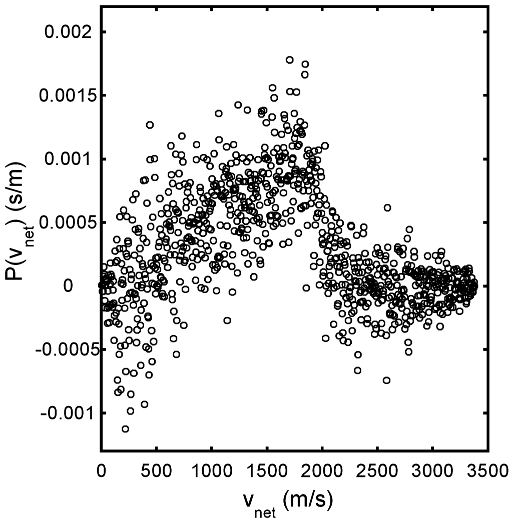

Figure 5. Speed distribution for m/z = 42 (CH_2CO^+) fragments derived from the ion image.

words, regardless of the amount of secondary recoil kinetic energy imparted, the resultant net velocity of ketene is nearly identical to the velocity of the vinoxy radical that dissociates to H + ketene. Consequently, we used the measured net speed distribution of ketene to approximate the $P(v)$ of all vinoxy radicals that dissociated to H + ketene products. The resultant $P(E_T)$ calculated from this speed distribution is depicted in green trace in Figure 6. We can thus compare the total Cl + vinoxy $P(E_T)$ to the portion that produces vinoxy radicals that dissociated to H + ketene products. We assumed all of the ketene is from vinoxy generated from C–Cl photofission, so the $P(E_T)$ in green shows the portion of the C–Cl photofission events that gives vinoxy radicals which dissociate to H + ketene products. The total primary $P(E_T)$ is shown in black trace in Figure 6 for comparison. The "ketene" portion was scaled to the same height as that predicted by the ratio calculated in Section IIID. In this way, we account for the fact that vinoxy can also dissociate via channel (2). Comparing the two traces in the figure, their shapes are fairly similar in the region between 10 and 25 kcal/mol and appear relatively flat. This suggests that the branching fraction to the H + ketene channel is roughly constant for vinoxy radicals produced from events within this range of relative translational energy (where C–Cl fission produced internally hot vinoxy radicals). In the higher kinetic energy portion of the $P(E_T)$, where vinoxy is produced with lower vibrational energies, the dissociation to H + ketene drops off. Analyzing this portion of the spectrum gives us important information on the relative barriers for dissociation to H + ketene as compared to isomerization and dissociation to CH_3 + CO. This analysis is described in the following section.

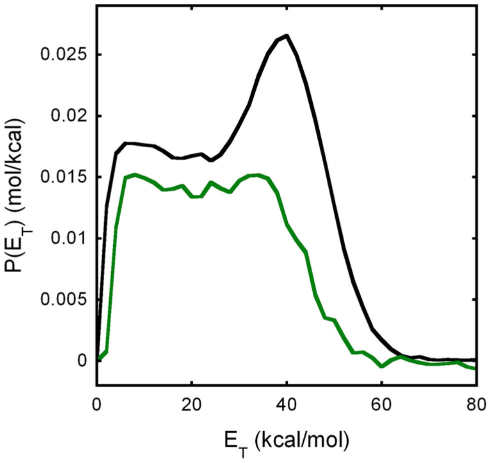

Figure 6. Green trace is the portion of the total primary $P(E_T)$ that leads to H + ketene products upon secondary dissociation derived from the measured $P(v_{net})$ of m/z = 42 (CH_2CO^+), assuming the additional velocity imparted to the ketene upon secondary dissociation via C–H bond fission is small (see text). The black trace is the total primary $P(E_T)$ (from Figure 4) shown for comparison. The "ketene portion" is scaled using the results of the branching calculations at model E_T values (see Figure 10).

D. Predicting the Product Branching for Vinoxy Radicals Produced from C–Cl Photofission. To compare our measured ketene speed distribution (which gives the speed distribution of vinoxy radicals that dissociate to H + ketene) to that predicted from RRKM calculations using the total C–Cl bond fission $P(E_T)$, we must account for the partitioning of the internal energy of the vinoxy radical between rotational and vibrational energy. When C–Cl fission imparts high relative kinetic energies to Cl + vinoxy, the vinoxy radicals are formed with high rotational energies. To determine the rotational angular momentum of the vinoxy radical, we used a model developed by our group in refs 15 and 16, summarized here. The rotational model uses angular momentum conservation to predict the angular momentum imparted to the radical moiety upon the cleavage of the C–Cl bond. Neglecting the angular momentum of the photon and the electronic angular momentum of the products (assumed to be negligible), the supersonic expansion of the molecular beam should rotationally cool the chloroacetaldehyde thus giving it an initial angular momentum of essentially zero. After the dissociation, the total angular momentum of the fragments must be zero as well.

$$\vec{J}_{\mathrm{tot}} = \vec{J}_{\mathrm{orb}} + \vec{J}_{\mathrm{rot}} = \vec{0} \tag{6}$$

Here $\vec{J}_{\mathrm{orb}}$ represents the orbital angular momentum of the Cl + vinoxy fragments, and $\vec{J}_{\mathrm{rot}}$ represents the rotational angular momentum of the vinoxy radical. Thus, $\vec{J}_{\mathrm{rot}}$ is equal in magnitude and opposite in direction to $\vec{J}_{\mathrm{orb}}$, which can be calculated classically. Since the impulsive force is along the C–Cl bond, the rotational angular momentum can be calculated using

$$-\vec{J}_{\mathrm{rot}} = \vec{J}_{\mathrm{orb}} = \vec{r} \times \mu \vec{v}_{\mathrm{rel}} \tag{7}$$

where $\vec{r}$ is the vector between the center of mass of the radical moiety in the precursor and the Cl atom, μ is the reduced mass of the radical and Cl system, and $\vec{v}_{\mathrm{rel}}$ is the relative velocity vector. Assuming the repulsive force within the Franck–Condon region of the excited-state potential acts along the C–Cl bond, the direction of $\vec{v}_{\mathrm{rel}}$ is oriented along the C–Cl bond, and the magnitude of $\vec{v}_{\mathrm{rel}}$ is determined from the measured relative translational energy imparted to the Cl atom and the vinoxy radical, E_T. So, all of the terms can be calculated from the equilibrium geometry of chloroacetaldehyde and the measured relative translational energy. The rotational energy of the radical is then given by

$$E_{\mathrm{rot}} = \frac{1}{2}\vec{J}_{\mathrm{rot}}^{\,T} I^{-1} \vec{J}_{\mathrm{rot}} \tag{8}$$

where $\vec{J}_{\mathrm{rot}}^{\,T}$ is the transpose of the angular momentum vector, and I^{-1} is the inverse of the inertia tensor. Thus, we can account for the dependence of the rotational energy imparted to the radical from the C−Cl bond photodissociation on the relative translational kinetic energy. Therefore, this model predicts the ratio of rotational energy to translational energy ($E_{\mathrm{rot}}/E_{\mathrm{T}}$) simply using the geometry of chloroacetaldehyde.

The geometry of the radical moiety formed from chloroacetaldehyde is different from the equilibrium geometry of the radical, and so the two will have different inertia tensors. Since the rotational angular momentum vector, $\vec{J}_{\mathrm{rot}}$, is constant in both magnitude and direction, the two geometries will also have different rotational energies according to eq 8. The same can be said about any other stationary point along the PES, such as the transition states or other minima. By preserving the angular momentum vector from its orientation in the radical moiety and changing the geometry to that of the stationary point, we can account for the different inertia tensor and obtain the $E_{\mathrm{rot}}/E_{\mathrm{T}}$ ratios for any stationary point. This can also be applied to points along a reaction coordinate, thus giving an $E_{\mathrm{rot}}/E_{\mathrm{T}}$ ratio at each point; this determines how the rotational energy changes as the radical changes its geometry from the equilibrium geometry of vinoxy to the geometries at the isomerization barrier to acetyl or at the TS for dissociation to H + ketene. For the calculations at the minimum or at the two TSs, we use geometries directly outputted from geometry optimization calculations (or IRC calculations) that are generally put into a "standard orientation" by rotating the coordinate system. This difference in the coordinate system between the points makes it incorrect to directly take the vector from its orientation in the radical moiety and superimpose it onto the geometry of interest. To account for this change, we transform the angular momentum vector into the coordinate system used for the relevant standard orientation thus ensuring that the vector has the same magnitude and orientation relative to the molecule. For more detail, see the Supporting Information.

The main goal of the calculations described here was to predict the portion of the primary $P(E_{\mathrm{T}})$ that produces vinoxy radicals that dissociate to H + ketene versus methyl + CO, giving us a predicted branching ratio at each measured E_{T} value. From our rotational model, we see that the rotational energy imparted to the radical changes as it reaches a barrier en route to products. The sum of the vibrational, rotational, and potential energy at any geometry must equal the total internal energy of the vinoxy radical at equilibrium geometry, so if the rotational energy decreases en route to the TS, there is more energy available to surmount the barrier to the reaction. Thus, to calculate the correct density of vibrational states at the equilibrium geometry for an RRKM rate constant and the correct sum of states at the TS, one must account for this change in rotational energy to calculate the unimolecular rate constant.

Figure 7 shows a diagram of the energetics involved in a general unimolecular reaction. The total energy in the radical, E^*, consists of rotational energy, E_{rot}, and vibrational energy, E_{vib}, while the total energy at the TS, $E^{\ddagger}$, consists of both rotational and vibrational energy, $E_{\mathrm{rot}}^{\ddagger}$ and $E_{\mathrm{vib}}^{\ddagger}$, as well as translational energy along the reaction coordinate, $E_{\mathrm{t}}^{\ddagger}$. The barrier height, E_{o}, is defined as the energy difference between the zero-point corrected minimum energy of the radical and the zero-point corrected energy of the TS (this is the G4 barrier height). Thus, $E^* - E_{\mathrm{o}} = E^{\ddagger}$. If we want to account for the effect that E_{rot} and $E_{\mathrm{rot}}^{\ddagger}$ have on this picture, we must subtract them from E^* and $E^{\ddagger}$, respectively, so that we calculate the correct density of vibrational states at the reactant and the correct sum of states in the orthogonal degrees of freedom at the TS. Since most RRKM calculations only use thermal distributions of rotational energies, we introduce an "effective barrier" to allow us to calculate the density and sum of vibrational states at the right energies, E_{vib} and $E_{\mathrm{vib}}^{\ddagger}$. We thus define the "effective" energy in the TS, $E^{\ddagger}_{\mathrm{effective}}$, and the "effective barrier height", $E_{\mathrm{o,effective}} = E_{\mathrm{o}} + E_{\mathrm{rot}}^{\ddagger} - E_{\mathrm{rot}}$. If $E_{\mathrm{rot}}^{\ddagger}$ is greater than E_{rot}, then $E_{\mathrm{o,effective}}$ is greater than E_{o}; if $E_{\mathrm{rot}}^{\ddagger}$ is less than E_{rot}, then $E_{\mathrm{o,effective}}$ is less than E_{o}. This correctly adjusts $E_{\mathrm{vib}}^{\ddagger}$ as needed. A decrease in the rotational energy en route to the TS makes the barrier easier to cross. Therefore, we use the effective barrier height and $E_{\mathrm{vib}} = E^*$ as our input to an RRKM calculation to correctly predict the branching fraction to the two product channels.

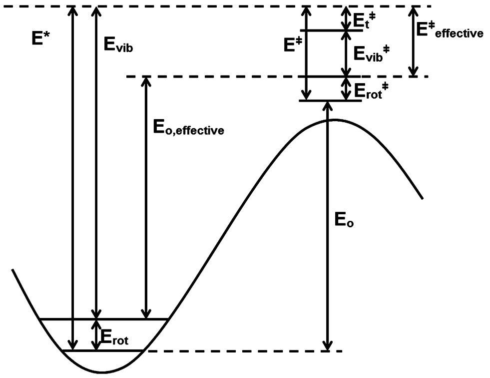

Figure 7. Diagram of the energies involved in a general unimolecular reaction. E^* is the total internal energy in the radical, which consists of vibrational energy, E_{vib}, and rotational energy, E_{rot}. $E^{\ddagger}$ is the total internal energy at the critical configuration, which consists of vibrational energy, $E_{\mathrm{vib}}^{\ddagger}$, rotational energy, $E_{\mathrm{rot}}^{\ddagger}$, and the translational energy along the reaction coordinate, $E_{\mathrm{t}}^{\ddagger}$. E_{o} is the energy difference between the zero-point energy of the radical and that of the critical configuration, thus representing the barrier height. We are concerned with the "effective" barrier height, $E_{\mathrm{o,effective}}$, which is the energy difference between the zero-point energy of the radical plus E_{rot} and the zero-point energy of the critical configuration plus $E_{\mathrm{rot}}^{\ddagger}$. Note that if $E_{\mathrm{rot}}^{\ddagger}$ is greater than E_{rot}, then $E_{\mathrm{o,effective}}$ is greater than E_{o}; if $E_{\mathrm{rot}}^{\ddagger}$ is less than E_{rot}, then $E_{\mathrm{o,effective}}$ is less than E_{o}. The effective energy in the critical configuration, $E^{\ddagger}_{\mathrm{effective}}$, then consists of $E_{\mathrm{t}}^{\ddagger}$ and $E_{\mathrm{vib}}^{\ddagger}$.

Our rotational model is used to characterize the rotational energy of the radical, E_{rot}, and TS, $E_{\mathrm{rot}}^{\ddagger}$, for the channel of interest. Since the energies we get from the model are then used to calculate E_{vib} and $E_{\mathrm{o,effective}}$, there are two points that need to be made about using our rotational model. The first point is that the rotational energy imparted to the radical upon dissociation depends on the geometry of the precursor. The conformers of chloroacetaldehyde have the Cl atom oriented at different dihedral angles to the O−C−C plane, and therefore, the repulsive force will impart an angular momentum vector to the moiety that is different for each conformer. So, we consider each conformer separately and sum their respective contributions in the end. The second point is that the rotational energy imparted to the radical or at any other stationary point depends on the recoil translational energy. For each E_{T} in the measured

C−Cl bond fission $P(E_T)$, we calculate a value for E_{rot} from the E_{rot}/E_T ratio for the radical and calculate a value for $E_{rot}^{\ddagger}$ from the E_{rot}/E_T ratio for the TS. Since these energies are used to calculate the effective barrier height and both depend on E_T, the effective barrier height depends on E_T as well. For instance, a radical formed from a C−Cl bond fission event with an E_T value of 4 kcal/mol will have a different effective barrier height compared to one formed from C−Cl bond fission that imparted an E_T value of 18 kcal/mol. Therefore, we need to consider the effective barrier heights for each value of E_T in the primary $P(E_T)$.

The first part of the branching calculations involved calculating the effective barrier heights for the H + ketene and methyl + CO product channels. Since the barrier for the isomerization to acetyl is much larger than the subsequent barrier to form the methyl + CO products, we treat the isomerization barrier as a bottleneck for this channel and assume that any vinoxy radicals that form acetyl go on to produce methyl + CO. The E_{rot}/E_T ratios at each geometry along the IRC for a given channel were calculated from the rotational model and multiplied by the values of E_T in the measured primary $P(E_T)$ to obtain the rotational energy at each geometry. Rotationally corrected IRCs were then constructed by adding the rotational energy to the B3LYP energies from the IRC with $\vec{J}_{rot} = 0$. An example set of rotationally corrected IRCs showing both channels and with the anti conformer geometry of the precursor used in the rotational model are shown in Figure 8. Although it is difficult to see in the figure, the energy difference between the two barriers decreases as E_T increases, and the effective barrier heights both decrease as E_T increases. Both of these trends demonstrate the effects of rotational energy on the statistical prediction for the product branching. The effective barrier height is the energy difference between the saddle point and minimum energy geometry on the rotationally corrected IRC. We could simply subtract the energies at those points in the rotationally corrected IRC to get the effective barrier height, but these energies were calculated at a lower level of theory and thus will not accurately predict the barrier. However, we can use the G4 barrier heights and then make corrections to those using the E_{rot}/E_T ratios at the minimum and transition state instead. So, we find that

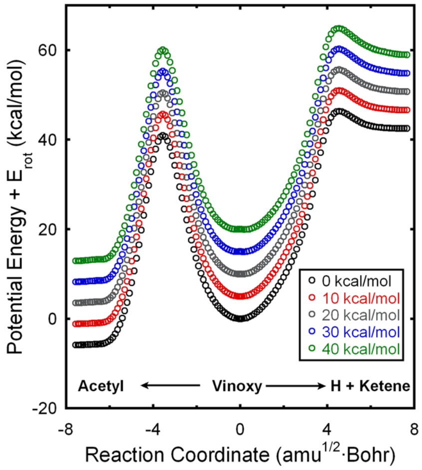

Figure 8. Example of the rotationally corrected IRCs for the unimolecular dissociation of the vinoxy radical to H + ketene and isomerization of the vinoxy radical to the acetyl radical. Each curve shows the resulting corrected IRC if the energy given in the legend is the E_T imparted during C−Cl photofission. The label at the bottom of the plot indicates which products/intermediate is formed moving in one direction along the reaction coordinate. Energies are not zero-point corrected, and the rotational model used the anti conformer of the precursor.

$$E_{o,effective} = E_o + \left[\left(\frac{E_{rot}}{E_T}\right)_{at\ TS} - \left(\frac{E_{rot}}{E_T}\right)_{at\ min}\right]E_T \tag{9}$$

where $E_{o,effective}$ is the effective barrier height, E_o is the G4 barrier height, and $\left(\frac{E_{rot}}{E_T}\right)_{at\ TS}$ and $\left(\frac{E_{rot}}{E_T}\right)_{at\ min}$ are the E_{rot}/E_T ratios at the TS and minimum energy points on the IRC, respectively. However, the rotational corrections can actually cause the minimum or saddle point to shift to another geometry along the IRC, usually nearby. We account for this in the effective barrier height (see Supporting Information). In summary, we have the effective barrier heights for each channel at all E_T values in the primary $P(E_T)$. For completeness, the enantiomers of the two TSs (see Supporting Information) were also considered giving four sets of effective barrier heights: two for the isomerization (and thus formation of methyl + CO products) and two for the formation of H + ketene products.

The second part of the calculations involved characterizing the vibrational energy of the radicals. Since the effective barrier heights depend on E_T, vinoxy radicals produced from C−Cl photodissociation with different E_T values have different reaction dynamics. Thus we calculated the vibrational energy of the radicals produced at small increments in E_T within the primary $P(E_T)$. To calculate E_{vib} for vinoxy radicals produced from C−Cl photodissociation, we used the following equation

$$E_{vib} = h\nu + E_{int}(\text{precursor}) - D_o(\text{C−Cl}) - E_{int}(\text{Cl}) - \left[1 + \left(\frac{E_{rot}}{E_T}\right)_{vinoxy}\right]E_T \tag{10}$$

which involves conservation of energy, like eq 4, and approximates the rotational energy in the radical with the E_{rot}/E_T ratio from our rotational model. While it is possible to use average values or the value at the equilibrium geometry for the terms in eq 10, we considered the range of possible values of E_{int}(precursor) and E_{rot}/E_T of vinoxy by determining the distributions for each, $P(E_{int}(\text{precursor}))$ and $P(E_{rot}/E_T)$. Since the internal energy of the Cl atom must be subtracted from the total internal energy to get the vibrational energy of the momentum matched vinoxy radical, we separately determined the velocity distribution of the Cl atoms in each spin−orbit state in our experiment.

Assuming the supersonic expansion of the molecular beam cools the rotational energy of the precursor, E_{int}(precursor) is composed of mostly vibrational energy, and so we can approximate $P(E_{int}(\text{precursor}))$ using Maxwell−Boltzmann statistics taking the molecules to be in thermal equilibrium with the nozzle. We first used the Beyer−Swinehart algorithm[30,31] to determine the vibrational degeneracy within a small range about a given E_{vib}. For each E_{vib}, the degeneracy is then weighted by the respective Boltzmann factor to produce $P(E_{int}(\text{precursor}))$. The Beyer−Swinehart algorithm used the vibrational frequencies of the precursor conformer of interest and an energy grain of 0.1 cm^{-1}. The counts are binned in 0.1

kcal/mol increments centered at each E_{vib}. The average internal energy calculated from this predicted distribution is in good agreement with the values predicted from statistical mechanics.

As for $P(E_{\mathrm{rot}}/E_{\mathrm{T}})$, the nuclear configuration of the precursor changes as it vibrates along any of its normal modes of vibration, and so the $E_{\mathrm{rot}}/E_{\mathrm{T}}$ ratio depends on the instantaneous geometry of the precursor along the vibrational mode. Using our rotational model, we can calculate $E_{\mathrm{rot}}/E_{\mathrm{T}}$ imparted at various vibrational displacements from equilibrium along a given normal mode of chloroacetaldehyde. To find the value of $P(E_{\mathrm{rot}}/E_{\mathrm{T}})$, we approximated the probability of finding the precursor with that displacement using the square of the harmonic vibrational wave function and then made the appropriate Jacobian corrections. The vibrational mode for the conformer of interest that produced the largest change in $E_{\mathrm{rot}}/E_{\mathrm{T}}$ at the classical turning points was chosen for this analysis, and the range of displacements extended beyond the classical turning points for the mode.

Using eq 10 and by convolving $P(E_{\mathrm{int}}(\mathrm{precursor}))$ and $P(E_{\mathrm{rot}}/E_{\mathrm{T}})$ together, a vibrational energy distribution, $P(E_{\mathrm{vib}})$, for vinoxy radicals from C−Cl photodissociation with a given E_{T} can be constructed. To finally account for the spin−orbit coupling of Cl, separate $P(E_{\mathrm{vib}})$s were made for vinoxy radicals produced from C−Cl photodissociation with $\mathrm{Cl}(^2\mathrm{P}_{3/2})$ and with $\mathrm{Cl}(^2\mathrm{P}_{1/2})$ as the cofragment by taking the internal energy of Cl to be either 0 or 2.5 kcal/mol, respectively. These $P(E_{\mathrm{vib}})$s were then scaled by the relative probability of producing vinoxy and the respective spin−orbit state from C−Cl bond fission with that given range of E_{T} using the weighted $P(E_{\mathrm{T}})$s for each process. The contributions were then added together to produce a total $P(E_{\mathrm{vib}})$ at a given E_{T}. Both $P(E_{\mathrm{int}}(\mathrm{precursor}))$ and $P(E_{\mathrm{rot}}/E_{\mathrm{T}})$ were normalized before calculating $P(E_{\mathrm{vib}})$ to ensure it would be normalized after the convolution (but prior to scaling). $P(E_{\mathrm{vib}})$ values were binned in E_{vib} increments of 0.1 kcal/mol, which is smaller than the E_{T} increment of the weighted $P(E_{\mathrm{T}})$s. The weighted $P(E_{\mathrm{T}})$s for photodissociation events leading to $\mathrm{Cl}(^2\mathrm{P}_{3/2})$ and $\mathrm{Cl}(^2\mathrm{P}_{1/2})$ were used here to account for the branching ratio as well as the number of radicals produced from photodissociation events with that range of E_{T}. These distributions were smoothed and interpolated from the data using the method previously described and are incremented the same as the primary $P(E_{\mathrm{T}})$ for all dissociation events.

The final part of the calculations used RRKM calculations to determine the product branching. From the previous parts, we now have a $P(E_{\mathrm{vib}})$ for vinoxy radicals and an effective barrier height at each value of E_{T} in the primary $P(E_{\mathrm{T}})$. At a given E_{T} value, we calculated the RRKM rate constant for each channel using the E_{vib} values from the $P(E_{\mathrm{vib}})$, the effective barriers for that channel, and the vibrational frequencies for the TSs leading to the products. Since there are two channels to each set of products, we summed the rate constants for the channels going to the same products giving us k_{iso} for the total rate constant of isomerization channel and k_{Hloss} for the total rate constant of the H + ketene channel. To get the branching fraction to each channel for unstable vinoxy radicals at a given E_{vib}, we calculated the fraction $k_{\mathrm{iso}}/k_{\mathrm{tot}}$ and $k_{\mathrm{Hloss}}/k_{\mathrm{tot}}$ where $k_{\mathrm{tot}} = k_{\mathrm{iso}} + k_{\mathrm{Hloss}}$. Once we have the branching fraction for every value of E_{vib} in $P(E_{\mathrm{vib}})$ for a given E_{T}, we then get a branching fraction at that E_{T} to each channel by discretely integrating the product of the $P(E_{\mathrm{vib}})$ and $k_{\mathrm{iso}}/k_{\mathrm{tot}}$ or $k_{\mathrm{Hloss}}/k_{\mathrm{tot}}$ over all of the E_{vib} values.

$$\text{branching to CH}_3 + \text{CO (via isomerization)} = \int_{E_{\mathrm{vib},i}}^{E_{\mathrm{vib},f}} P(E_{\mathrm{vib}}) \frac{k_{\mathrm{iso}}}{k_{\mathrm{tot}}} \mathrm{d}E_{\mathrm{vib}} \tag{11}$$

$$\text{branching to H + ketene} = \int_{E_{\mathrm{vib},i}}^{E_{\mathrm{vib},f}} P(E_{\mathrm{vib}}) \frac{k_{\mathrm{Hloss}}}{k_{\mathrm{tot}}} \mathrm{d}E_{\mathrm{vib}} \tag{12}$$

We then determined the portion of the radicals leading to either H + ketene or methyl + CO products by multiplying the branching fraction at each E_{T} by the experimentally determined $P(E_{\mathrm{T}})$ value for the unstable vinoxy radicals at that E_{T}. Doing this for all of the E_{T} values in the $P(E_{\mathrm{T}})$ thus gave us the portion of the primary $P(E_{\mathrm{T}})$ that we predict to give vinoxy radicals that then dissociate to form each set of products. This can then be directly compared to the measured H + ketene distribution in green in Figure 6. The next section shows this prediction using the G4 barriers calculated for each TS. We then investigate how increasing the barrier to H + ketene improves the agreement with the experimental results.

As previously mentioned, we needed to consider the conformers of the precursor separately since the angular momentum vector imparted to the radical in the photodissociation depends on the geometry of the precursor. To account for the conformers of chloroacetaldehyde, the calculations were run for each conformer using the C−Cl bond fission $P(E_{\mathrm{T}})$s for photodissociation events leading to $\mathrm{Cl}(^2\mathrm{P}_{3/2})$ and $\mathrm{Cl}(^2\mathrm{P}_{1/2})$ (Figure 3) scaled by the relative population of that conformer in the molecular beam. This provided us with the contributions of the conformers to the portions of the C−Cl fission $P(E_{\mathrm{T}})$ forming vinoxy radicals that dissociate to form H + ketene and methyl + CO. The contributions from each conformer to the portions were then summed together to give the total portions. While there are technically two anti conformers for chloroacetaldehyde, both produced identical contributions when run separately, and so we are able to describe the dynamics of both using only one of the geometries.

E. Comparison of Branching Predictions with Measured Ketene Speed Distribution. The results of the branching calculations using the calculated G4 barrier heights for both channels are shown in Figure 9. In the upper frame, the red dashed line shows the portion of the primary C−Cl fission $P(E_{\mathrm{T}})$ leading to vinoxy radicals that produce H + ketene products, and the blue dashed line shows that producing methyl + CO products. The primary $P(E_{\mathrm{T}})$ is shown in black solid line for reference, and the portion of the $P(E_{\mathrm{T}})$ representing vinoxy radicals that are stable to secondary dissociation is shown in dashed gray line (this was obtained by subtracting the portions leading to the two sets of products from the primary $P(E_{\mathrm{T}})$). From this figure, it looks as though the production of ketene dominates at lower E_{T} values (i.e., higher E_{vib} values); the contribution from vinoxy radicals going to methyl + CO products is low at lower E_{T} values and gradually increases. Stable vinoxy radicals dominate at E_{T} values greater than 50 kcal/mol.

As previously mentioned, the recoil kinetic energy imparted in the dissociation of vinoxy to H + ketene is expected to have little effect on the net speed of ketene given the large mass difference between the fragments. This allowed us to approximate the speed distribution of the vinoxy radicals that

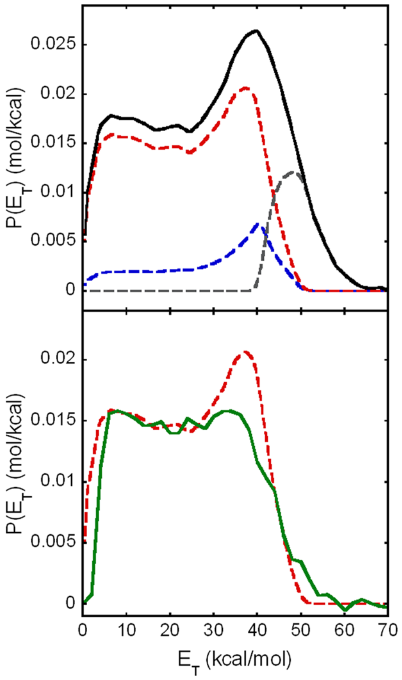

Figure 9. Results of the branching calculations using the calculated G4 barrier height (42.2 kcal/mol) for the H loss channel. The upper frame shows the total primary $P(E_T)$ (solid black curve) along with the predicted portions that produce H + ketene products (dashed red curve), methyl + CO products (dashed blue curve), and stable vinoxy radicals (dashed gray curve). The "stable" portion of the $P(E_T)$ is the distribution of C−Cl photofission events that our model predicts partitions insufficient vibrational energy to surmount the 40.6 kcal/mol isomerization barrier to acetyl (the lowest barrier en route to dissociation). The lower frame shows a comparison of the experimental (solid green curve) and predicted (dashed red curve) portion of the primary $P(E_T)$ that results in H + ketene products. The experiment portion has been scaled to match the predicted portion and is the same curve depicted in Figure 6. Note how the branching calculations predict more vinoxy radicals producing H + ketene at higher translational energies than the experimental portion shows.

dissociate to H + ketene from the experimental speed distribution of ketene and thus derive a measured $P(E_T)$ for vinoxy radicals that produce ketene. This experimental result is shown in green line in Figure 6. Our branching calculations predict a $P(E_T)$ for vinoxy radicals that produce ketene, and so we can compare the measured ketene portion to that predicted from our RRKM calculations using the G4 barrier of 42.2 kcal/mol. We show both the predicted and experimental ketene portions in dashed red line and solid green line, respectively, in the lower frame of Figure 9 for comparison. The measured ketene portion was scaled relative to the predicted portion in range of E_T from 5−15 kcal/mol, where we expect the branching to remain relatively constant. While the lower E_T values give a decent agreement to the experiment, the calculations predict too much ketene at higher E_T values near 40 kcal/mol, where the vibrational energy in the vinoxy radical is near the calculated threshold for dissociation to H + ketene.

To resolve the disagreement between the measured and predicted portion of the $P(E_T)$ leading to ketene using the calculated G4 barrier heights for both channels, we decided to alter the barrier height used in our calculation to improve the comparison. In our branching calculations, the effective barrier heights for a given channel are determined by correcting the G4 barrier height for the channel based on the rotationally corrected IRCs. However, we can choose to use a barrier height for a channel that is different from the calculated G4 barrier height. Assuming the new barrier height would not significantly affect the minima and overall shape of the IRC, we can still use it to make the rotational corrections to this new barrier height and get effective barrier heights from it. We therefore ran our branching calculation changing only the H + ketene barrier height to try to get a ketene portion that better agreed with the measured ketene portion. The best agreement came from using a barrier height of 44.6 kcal/mol for the H + ketene channel; the results of the branching calculation for this barrier height are shown in Figure 10. The upper frame shows the portions of the primary C−Cl fission $P(E_T)$ that produce vinoxy that dissociates to H + ketene and methyl + CO products along with the portion that is stable to secondary dissociation. There is clearly less production of ketene at higher values of E_T than we saw with the calculated G4 barrier height, and production of methyl now dominates in the E_T range of 40 to 52 kcal/mol. In the bottom frame, we see that the measured and predicted portions that produce ketene agree much more

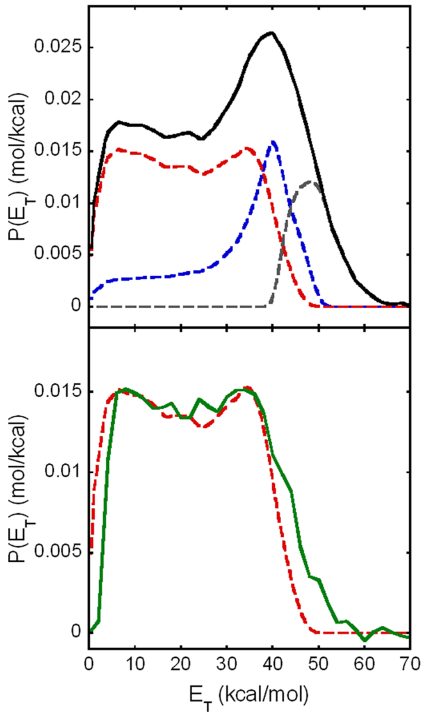

Figure 10. Results of the branching calculations using a barrier height of 44.6 kcal/mol for the H loss channel. The upper frame shows the total primary $P(E_T)$ (solid black curve) along with the predicted portions that produce H + ketene products (dashed red curve), methyl + CO products (dashed blue curve), and stable vinoxy radicals (dashed gray curve). The "stable" portion of the $P(E_T)$ is the distribution of C−Cl photofission events that our model predicts partitions insufficient vibrational energy to surmount the 40.6 kcal/mol isomerization barrier to acetyl (the lowest barrier en route to dissociation). The lower frame shows a comparison of the experimental (solid green curve) and predicted (dashed red curve) portion of the primary $P(E_T)$ that results in H + ketene products. The experiment portion was scaled to match the predicted portion and is the same curve depicted in Figure 6. The experimental and predicted portions agree much better using this barrier height than the calculated G4 barrier height.

closely, as there is no longer too much ketene predicted at higher E_T values near 40 kcal/mol. These results suggest that the difference in energy between the barrier to H + ketene and the isomerization barrier en route to CH_3 + CO is underestimated in the G4 results; the best fit to our data results from using a H + ketene barrier that is ∼4.0 ± 0.5 kcal/mol higher than the isomerization barrier.

F. Detection of Methyl Radical, CH_3. Our study on the product branching in the unimolecular dissociation of vinoxy can never be conclusive without detecting neutral methyl radicals yielded from channel (2). We use 10.5 eV photoionization to probe CH_3, accumulating data at $m/z = 15$. The recorded image is converted to a net speed distribution, shown in Figure 11. The signal at $m/z = 15$ is marginally detectable, and thus the signal-to-noise ratio of the $P(v_{net})$ is unsatisfactory. The $P(v_{net})$ spans a wide range of speeds making fitting very ambiguous. According to our previous work, vinoxy radicals prepared in the ground state by photolysis dissociate to produce methyl + CO products with negligible secondary recoil translational energy. Thus, a good fit for the fast part of the $P(v_{net})$ we present here cannot be achieved without imparting an exaggerated amount of secondary recoil translational energy. This leads us to ascribe the fastest part of $m/z = 15$ to the dissociative ionization of vinoxy radicals.

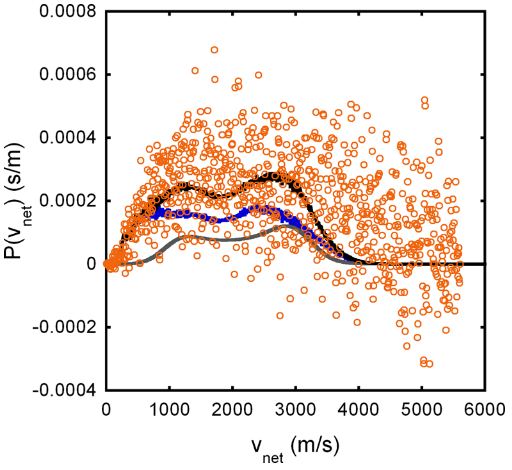

Figure 11. Speed distribution for $m/z = 15$ (CH_3^+) fragments derived from the ion image. The gray line is the predicted $P(v_{net})$ of CH_3^+ from the dissociative ionization of the stable vinoxy radicals. The v_{net} of the CH_3^+ is calculated from the vector sum of the stable vinoxy radical velocities using the $P(E_T)$ in gray in Figure 10 and a secondary recoil estimated from ref 32. The blue line is the predicted $P(v_{net})$ of the methyl formed in the neutral dissociation of vinoxy radicals. It is calculated from the vector sum of the velocities of the vinoxy radicals that dissociate to CH_3 + CO (using the blue portion of the $P(E_T)$ in Figure 10), and a secondary recoil translational energy distribution. The secondary $P(E_T)$ is a half-normal distribution peaked at 0 kcal/mol with a σ-value of 5 kcal/mol. The black line is the sum of the two contributions.

To characterize the dissociative ionization of vinoxy to form methyl cations, we used the model developed by Brynteson and Butler,[32] which predicts the angular distribution and secondary recoil translational energy relative to the primary E_T for a barrierless dissociation channel. To model the CH_3^+ for dissociative ionization of vinoxy, the model predicts a $P(v_{net})$ for CH_3^+ by vector addition of the velocity of the stable vinoxy radical being photoionized and the velocity imparted to the CH_3^+ during the dissociative ionization. Since Gaussian calculations done on the cationic surface of vinoxy suggest that the exit channel for CH_3^+ + CO is a straight dissociation, we expect this model to work well for our system. The gray line in Figure 11 shows the predicted $P(v_{net})$ from the model using the portion of the $P(E_T)$ representing stable vinoxy radicals from our branching calculations with a H + ketene barrier height of 44.6 kcal/mol (dashed gray line in Figure 10). This predicted $P(v_{net})$ had been scaled by the amount of dissociation events in the primary $P(E_T)$ that lead to stable vinoxy and the product yield of the dissociative ionization estimated from the relative photoionization cross section of CH_3 to CH_3^+ and vinoxy to CH_3^+ reported by Osborn et al.[27] Since the model predicts too small a width for the secondary recoil translational energy distribution when $\vec{J}$ is near a principle axis, so the ratio between secondary E_T and the primary E_T is sharply peaked, we broadened the predicted $P(v_{net})$ by convolving it with a Gaussian function to try to account for the real spread in the secondary $P(E_T)$.

To predict the $P(v_{net})$ representing methyl radicals produced from secondary dissociation of neutral vinoxy, we used the forward convolution procedure described by Alligood et al.[33] We use the portion of the $P(E_T)$ representing vinoxy that then dissociates to methyl + CO from our branching calculations that best matched the measured data for ketene (dashed blue line in Figure 10). Assuming forward−backward scattering and a secondary recoil translational distribution represented by a half-normal distribution peaked at 0 kcal/mol with a σ-value of 5 kcal/mol, we get the predicted $P(v_{net})$ shown in blue line in Figure 11 (in the calculation, each primary velocity was scaled by the amount of dissociation events from the primary $P(E_T)$ that led to methyl products). The Gaussian function was peaked at 0 kcal/mol to reflect the results of our previous study, and the width of 5 kcal/mol had to be added in order for the predicted $P(v_{net})$ to fit the data at slow speeds. Without considering strong forward−backward scattering in the secondary dissociation, the slow part of the $P(v_{net})$ could not be well fit either. The black line is the sum of the two traces, which gives an overall satisfactory fit but still cannot describe the observed signal at higher speeds.

IV. DISCUSSION

This study focused on characterizing the branching between the unimolecular dissociation channels of the vinoxy radical to H + ketene and methyl + CO products. We used a methodology similar to that in a previous study done by our group to generate vinoxy radicals, with high internal energies and under collision-free conditions, by photolysis of the precursor chloroacetaldehyde, but using 157 nm light instead of 193 nm light. We then looked for the ketene products and methyl products from the secondary dissociation of the nascent vinoxy to ascertain the branching between the two channels. Although the contamination in the methyl signal did not allow us to experimentally determine the branching ratio, the ketene signal provided key information on how the branching fraction to the H + ketene product channel changes with vibrational energy in the vinoxy radical. This offered a test of the relative barrier height for dissociation to H + ketene as compared to the isomerization and dissociation to CH_3 + CO. We find the data are best fit by assuming the barrier to H + ketene is ∼4.0 ± 0.5 kcal/mol higher than the isomerization barrier en route to CH_3 + CO, a difference larger than that predicted by G4 calculations of these barriers. The motivation for this study was the large discrepancy between the experimental and predicted branching found in the previous study, where the secondary dissociation of vinoxy was dominated by the methyl + CO channel with a negligible amount of ketene produced.

Our results show a marked change in the branching ratio between the two channels from the previous study. Not only do we see a substantial amount of ketene products that can be attributed to the secondary dissociation of the vinoxy radical but we also find a small amount of methyl as evidenced by the signal at m/z = 15. As opposed to the previous study, which was done with a much lower distribution of energies in the vinoxy radical, the secondary dissociation now favors the production of H + ketene over the production of methyl + CO products.

If we look at the internal energy in the radicals, we find that the vinoxy radicals produced from C−Cl bond fission of chloroacetaldehyde at 157 nm have higher internal energies compared to those produced in the previous study. This might be expected from the larger photon energy at 157 nm as compared to 193 nm. Interestingly, the majority of vinoxy radicals produced in this study have internal energies greater than 50 kcal/mol, while those in the previous study have internal energies lower than 50 kcal/mol. According to RRKM calculations, branching to the H + ketene channel dominates the methyl + CO channel when there is a great deal of vibrational energy in the radical, since the transition state for the H + ketene channel is looser than that for the isomerization channel. Therefore, the larger amount of ketene produced from secondary dissociation in this study is consistent with what we would expect from applying statistical TS theory to the H + ketene channel.

To treat the product branching more accurately, we note that the internal energy in the radical consists of both rotational and vibrational energy, and it is the vibrational energy, not the total energy, that allows one to surmount the barrier to each dissociation channel. Not only that, but changes in the rotational energy of the radical due to conservation of angular momentum as it moves along the PES can also affect the effective barrier heights (see Section IIID). Thus, our branching calculations account for the rotational energy in the vinoxy radical produced from C−Cl bond fission (using our rotational model) and how the rotational energy affects the dynamics of the radical. While the results of the calculations using the G4 barrier heights for the H + ketene channel and the isomerization channel to the acetyl radical (see Figure 9) agree with the data at most E_T values, there is a discrepancy at high E_T values near the threshold for production of H + ketene.

According to Young and Yarkony, nonadiabatic effects are not responsible for the previously observed suppression of the H + ketene channel; thus, we attempted to analyze our data here using statistical transition state theory without nonadiabatic recrossing. It is possible, then, that the negligible branching to H + ketene observed in the previous study by Miller et al. may be the result of a higher barrier for the H + ketene channel. While our G4 barrier heights are in good agreement with the previous G3//B3LYP, these barriers are not consistent with Miller's data nor with the internal energy dependence of the branching to H + ketene obtained in the current study. By running the calculations with a barrier height of 44.6 kcal/mol for the H + ketene channel as opposed to the G4 barrier height (see Figure 10), we were able to obtain a better agreement between the predicted and experimental ketene portions of the $P(E_T)$. This new barrier height is slightly above the barrier height predicted from the high-level ab initio calculations (43.0 kcal/mol) done by Bennett et al.[14] While this change in barrier height is relatively small, its effect can be rather large as only methyl production occurs at energies below the barrier to H + ketene and it still dominates the product branching for several kilocalories per mole above this higher H + ketene barrier height. Overall, the results of the branching calculations suggest that the data are consistent with secondary dissociation occurring along the ground electronic state PES, but the barrier height of the H + ketene channel is higher than predicted by the G4 method. The G4 results compared to in this experimental paper treat high-level correlation empirically, using parameters derived primarily from energy minima, not transition states. We are presently working to use advanced coupled cluster methods[34] to provide an ab initio determination of the barriers probed experimentally in this work. Note that our data are sensitive to the difference in the H + ketene barrier and the isomerization barrier, and the analysis relies on a C−Cl bond energy, so the robust conclusion is that the H + ketene barrier is 4.0 ± 0.5 kcal/mol above the isomerization barrier (44.6−40.6) if one assumes that the product branching is statistical.

In using statistical transition state theory for our branching model, we also assumed that tunneling does not contribute significantly to the branching between the channels. While the barrier to the H + ketene product channel is too broad for tunneling to be significant, tunneling through the isomerization channel to acetyl en route to CH_3 + CO is possible. However, most of our vibrational energy distribution is above this barrier, so we do not expect tunneling to contribute significantly to the branching to this channel. The very small fraction of radicals formed with vibrational energies just below the isomerization barrier might dissociate via tunneling on the time scale of the short delay between our photodissociation and ionization laser, but the analysis of the onset of the ketene + H product channel would be unaffected.

Because of the ambiguity in fitting the signal at m/z = 15, it is difficult to calculate a branching ratio between the two channels for this study from the experimental data. However, we can use the results of the branching calculations that best fit the signal at m/z = 42 to predict a branching ratio. Since we predicted the portions of the C−Cl bond fission $P(E_T)$ that produce vinoxy radicals which goes to either channel, we can simply integrate the area of these portions to find the amount of unstable vinoxy radicals that produce H + ketene and methyl + CO upon secondary dissociation. We therefore calculate a branching of ketene to methyl as ∼2.1:1. Using the photoionization cross sections of these species at 10.5 eV, we can also predict the ratio of the signal between the species, $\frac{N_{\text{ketene}^+}}{N_{\text{methyl}^+}}$. This ratio is ∼9, which suggests that the ketene signal should be ∼9 times greater than the methyl signal and would explain the low signal-to-noise for the m/z = 15 data. Since the appearance energy of fragments from ketene and methyl radical are well above the photoionization energy used in this experiment, we do not expect to lose any neutral ketene and methyl products to dissociative ionization.

Our analysis of the product branching in the unimolecular dissociation of vinoxy radicals relies on the assumption that C−Cl bond fission in chloroacetaldehyde at 157 nm produced vinoxy radicals that undergo internal conversion to the ground electronic state before they dissociate. The nascent vinoxy radicals are likely formed in the $\tilde{A}$ and $\tilde{B}$ excited electronic states, but they can of course internally convert to the ground-state PES via the avoided crossings and conical intersections calculated by Yarkony and co-workers. The primary C−Cl bond fission $P(E_T)$s for Cl($^2P_{3/2}$) and Cl($^2P_{1/2}$) are bimodal, with a high-kinetic-energy feature peaking near E_T = 40 kcal/mol in both that indicates dissociation along a repulsive energy surface. Both $P(E_T)$s also have a broad and slow feature, which is isotropic. Our energy and angular momentum constraints give onsets, shown in Figure 4, that suggest that the C−Cl photofission events that partition less than 19 kcal/mol to E_T can form nascent vinoxy radicals in the $\tilde{B}$ state, while most of the high-kinetic-energy component to the $P(E_T)$ peaking near 40 kcal/mol can produce vinoxy in the $\tilde{A}$ state but not in the $\tilde{B}$ state. We have undertaken EOM-CCSD calculations of the excited singlet and triplet states of chloroacetaldehyde; they are consistent with the assignment of the product channels. Our preliminary EOM-CCSD calculations with 6-311++G(3df,2p) basis are shown in the Supporting Information. The excited singlet state of chloroacetaldehyde with the highest oscillator strength is S_4; it is predissociated by a repulsive diabat at larger C−Cl distances and correlates adiabatically to Cl + vinoxy in the $\tilde{B}$ state. The S_3 state has a very similar vertical excitation energy as the S_4 state (~7.5 eV) but is strongly repulsive in the Franck−Condon region. It correlates adiabatically to Cl + vinoxy in the $\tilde{A}$ state. Thus, we infer that dissociation along the S_3 state likely results in the high-kinetic energy component of the C−Cl photofission $P(E_T)$, while dissociation along S_4 results in all or a portion of the low-kinetic-energy component of our $P(E_T)$ assigned to Cl + vinoxy in the $\tilde{B}$ state. The calculated triplet states of chloroacetaldehyde shown in the Supporting Information also include both repulsive and predissociative excited state accessed in the Franck−Condon region. We note that our model for predicting the angular momentum imparted during C−Cl bond fission assumes that the excited state is repulsive in the Franck−Condon region. Thus, it should accurately predict the angular momentum in the high-kinetic-energy portion of the bimodal $P(E_T)$ but not the low-kinetic portion. The branching ratio is only sensitive to the partitioning between rotational and vibrational energy in the high-kinetic-energy portion of the $P(E_T)$, so our model should correctly predict this partitioning in the region of the $P(E_T)$ that we have used for the barrier height determinations.

Finally, it is interesting to compare the dynamics on the repulsive excited singlet states of chloroacetaldehyde with that on the ^{1}E, ^{3}E, and Rydberg excited states of CH_3Cl. The Cl($^2P_{1/2}$)/Cl($^2P_{3/2}$) branching ratios and anisotropy parameters for the photodissociation of CH_3Cl have been studied at 193 nm by several groups as reviewed by Suits and co-workers[35] and at both 193 and 157 nm in Doppler measurements by Matsumi et al.[36,37] Although Matsumi et al. interpret their Doppler results at 157 nm as indicative of a bimodal C−Cl recoil kinetic energy distribution, more recent work by Lin et al.[38] detects a unimodal recoil kinetic energy distribution peaking near 85 kcal/mol; the Lin paper did not measure the Cl($^2P_{1/2}$)/Cl($^2P_{3/2}$) branching ratio or photofragment anisotropies. The Cl($^2P_{1/2}$)/Cl($^2P_{3/2}$) branching ratio for CH_3Cl excited at 157 nm was reported to be 0.65 ± 0.13[37] by Matsumi et al. but should be revised to ~0.9 using more recent REMPI line strength factors as discussed by Suits and co-workers. This compares closely with our measured Cl($^2P_{1/2}$)/Cl($^2P_{3/2}$) ratio for chloroacetaldehyde of 0.82 ± 0.16. The partial Cl($^2P_{1/2}$)/Cl($^2P_{3/2}$) branching ratio is smaller in the low-kinetic-energy component of our C−Cl photofission $P(E_T)$ and near unity in the high-kinetic-energy portion, so our high-kinetic-energy distribution evidences a similar Cl spin−orbit branching ratio to that observed for CH_3Cl at 157 nm. The Cl photofragement anisotropy is similar for both Cl($^2P_{1/2}$) and Cl($^2P_{3/2}$) in our data, weakly parallel (with an average β_2 of 0.23) in the high-kinetic energy portion of the $P(E_T)$ and isotropic in the low-kinetic energy portion. The weakly parallel anisotropy suggests optical excitation via both parallel and perpendicular transitions at 157 nm that each lead, presumably via nonadiabatic transitions en route, to both Cl($^2P_{1/2}$) and Cl($^2P_{3/2}$).

We fit the methyl signal from secondary dissociation in this work by assuming that a small amount of kinetic energy is imparted to the methyl fragment upon secondary dissociation of the vinoxy radical. If the secondary dissociation does occur on the ground-state PES, then we would expect a similar secondary $P(E_T)$ for this dissociation channel to that used in the study by Miller et al. While Miller et al. fit their methyl data assuming that the velocity imparted to the methyl product when vinoxy dissociated was negligible, a better fit was obtained for our data in this paper by assuming the secondary $P(E_T)$ peaked at 0 kcal/mol but increasing the spread in recoil kinetic energy imparted in the dissociation. We thus use a half-normal distribution for the secondary $P(E_T)$ for the dissociation of vinoxy to CH_3 + CO that has a σ-value of 5 kcal/mol. This difference may be a result of the much larger amount of energy in the vinoxy radical that can be imparted to the methyl radical. According to our branching calculations, we also find that the ketene data agree with the assumption that the secondary dissociation of vinoxy to H + ketene occurs on the ground-state PES (although we had to change the barrier height a bit). Despite vinoxy radicals possibly being produced in the $\tilde{A}$ state in this work, we thus make a similar assumption to that of Osborn et al., namely, that the radicals in excited states relax to the ground state where they then undergo secondary dissociation.

Much like in our results, the photodissociation of methyl vinyl ether at 193 nm also produced vinoxy radicals mostly in the $\tilde{A}$ state. Other similarities between the two studies include the production of vinoxy radicals with high internal energies (as well as a similar range of internal energies in the nascent vinoxy) and larger branching to H + ketene over CH_3 + CO. While we rationalized the larger branching to H + ketene by citing the higher internal energy in the vinoxy radical, this preferential branching to H + ketene products when vinoxy is formed in its $\tilde{A}$ state could instead result from a direct dissociation pathway on the $\tilde{A}$ state. A more extensive computational study of the dynamics on the $\tilde{A}$ state would be helpful in finding such a pathway and, if it exists, seeing how it competes with relaxation to the ground state.

While we assigned as much of the signal as we can, there are still possible issues with dissociative ionization of vinoxy. First, there is some discrepancy between the signal at m/z = 15 from dissociative ionization of the vinoxy radical to CH_3^+ in this study and that from the previous study on the photodissociation of chloroacetaldehyde at 193 nm. In the previous study, the contribution of dissociative ionization to the signal at m/z = 15 was determined to be negligible, whereas this study attributes a decent portion of the signal to this process. While the m/z = 15 appearance energy varies with the internal energy of the radical, G4 calculations on the cationic surface of vinoxy show that the barrier to forming CH_3^+ + CO is 10.4 eV from the minimum energy geometry of the vinoxy radical. This energy is consistent with the appearance energy of CH_3^+ for vinoxy found in a few references (10.3 eV),[27,28] and therefore photoionization at an energy above this appearance energy should give signal from stable vinoxy radicals at $m/z = 15$. It is therefore surprising that the previous chloroacetaldehyde study was able to fit the signal at $m/z = 15$ without a contribution from dissociative ionization. Experimental and theoretical work on the cationic surface of vinoxy would be beneficial in characterizing the dynamics on this surface and its contribution to the methyl signal.

Not only can vinoxy undergo dissociative ionization to form CH_3^+ + CO but it can also form H + CH_2CO^+. According to Lee et al.,[28] the dissociative ionization of vinoxy to H + CH_2CO^+ is significant when the photoionization energy is greater than 12.5 eV. Assuming this energy represents a barrier on the cationic surface to the formation of H + CH_2CO^+, stable vinoxy radicals with vibrational energies up to the isomerization threshold (40.6 kcal/mol) excited to the cationic surface using a photoionization energy of 10.5 eV would not have enough energy to surmount this barrier. In agreement with this analysis, Miller et al. found no evidence of dissociative ionization of stable radicals to $m/z = 42$, despite having a substantial number of radicals with vibrational energy near the isomerization threshold (using a slightly higher photoionization energy of 10.6 eV). We therefore do not expect any signal at $m/z = 42$ from the dissociative ionization of vinoxy to H + CH_2CO^+ using a photoionization energy of 10.5 eV. The only signal that Miller et al. did observe at $m/z = 42$ was from the ketene cofragment to HCl photoelimination. In the present work, the small unfit signal on the fast edge of the ketene portion in Figure 10 may be due to ketene from HCl photoelimination, which we consider in the Supporting Information. Minor HCl photoelimination channels have previously been detected by Lin et al.[38] for CH_3Cl at 157 nm.

V. CONLCUSION

This study detected the change in branching fraction to the H + ketene product channel of vinoxy radicals as the vibrational energy in the radical increases near the threshold to producing H + ketene. We find that the predicted portion of the $P(E_T)$ for C−Cl photofission in the precursor that produces vinoxy radicals that dissociate to H + ketene products best fits the experimental portion if we use a barrier height for the H + ketene channel that is 4.0 ± 0.5 kcal/mol higher than the isomerization barrier en route to CH_3 + CO products. This is a larger energy difference than that predicted by G4 calculations; it offers a benchmark for higher-level electronic structure determinations of these barriers. Our analysis assumes that statistical transition state theory adequately predicts the product branching. We introduce a method to explicitly account for the rotational energy (imparted to the vinoxy radicals produced photolytically) in the RRKM calculations, both at equilibrium geometry and at the relevant transition states for the product branching. This methodology can be extended to statistical predictions for the unimolecular dissociation of radicals produced photolytically from other halogenated precursors in experiments where the rotational distribution of the radicals are not relaxed to a thermal distribution.

■ ASSOCIATED CONTENT

Ⓢ Supporting Information

The Supporting Information is available free of charge on the ACS Publications website at DOI: 10.1021/acs.jpca.6b01256.

> The Supporting Information includes: (A) the geometries of the conformers of chloroacetaldehyde; (B) preliminary EOM-CCSD calculations of the excited states of chloroacetaldehyde; (C) analysis of the components in the C−Cl bond fission $P(E_T)$s for $Cl(^2P_{3/2})$ and $Cl(^2P_{1/2})$; (D) the speed dependence of the anisotropy parameter $\beta_2(v)$ for $Cl(^2P_{3/2})$ and $Cl(^2P_{1/2})$; (E) the correction to the effective barrier height caused by the shift of the minimum or saddle point to a nearby geometry along the IRC; (F) description of the permutation vectors used in our rotational model; (G) the E_T dependence of the branching fraction for the H + ketene and methyl + CO channels for the two major conformers; (H) an estimate of the $P(E_T)$ for a minor HCl elimination channel that is possible in this system, derived from the predicted and the experimental ketene $P(v_{net})$; and (I) the Gaussian convolution of the predicted $P(v_{net})$ for the methyl signal coming from the dissociative ionization of vinoxy to CH_3^+ + CO. (PDF)

■ AUTHOR INFORMATION

Corresponding Author

*E-mail: l-butler@uchicago.edu. Phone:773-702-7206.

Notes

The authors declare no competing financial interest.

■ ACKNOWLEDGMENTS

This work was supported by the Chemical Sciences, Geosciences and Biosciences Division, Office of Basic Energy Sciences, Office of Science, U.S. Department of Energy (DOE), under Grant No. DE-FG02-92ER14305 (L.J.B). During a no-cost extension of the DOE grant, the completion of the work was supported by the U.S. Army Research Laboratory and the U.S Army Research Office under Contract No. W911NF-14-1-0244. We thank P. Scrape for his help with implementing the excited-state calculations, notably the EOM-CCSD calculations, and his help with interpreting the results of the calculations.

■ REFERENCES

(1) Balucani, N.; Leonori, F.; Casavecchia, P.; Fu, B.; Bowman, J. M. Crossed Molecular Beams and Quasiclassical Trajectory Surface Hopping Studies of the Multichannel Nonadiabatic $O(^3P)$ + Ethylene Reaction at High Collision Energy. *J. Phys. Chem. A* **2015**, *119*, 12498−12511.

(2) Leonori, F.; Balucani, N.; Nevrly, V.; Bergeat, A.; Falcinelli, S.; Vanuzzo, G.; Casavecchia, P.; Cavallotti, C. Experimental and Theoretical Studies on the Dynamics of the $O(^3P)$ + Propene Reaction: Primary Products, Branching Ratios, and Role of Intersystem Crossing. *J. Phys. Chem. C* **2015**, *119*, 14632−14652.

(3) McKee, K. W.; Blitz, M. A.; Cleary, P. A.; Glowacki, D. R.; Pilling, M. J.; Seakins, P. W.; Wang, L. Experimental and Master Equation Study of the Kinetics of OH + C_2H_2: Temperature Dependence of the Limiting High Pressure and Pressure Dependent Rate Coefficients. *J. Phys. Chem. A* **2007**, *111*, 4043−4055.

(4) Westbrook, C. K.; Dryer, F. L. Chemical Kinetics and Modeling of Combustion Processes. *Symp. Combust., [Proc.]* **1981**, *18*, 749−767.

(5) Brezinsky, K. The High-Temperature Oxidation of Aromatic Hydrocarbons. *Prog. Energy Combust. Sci.* **1986**, *12*, 1−24.

(6) Barnhard, K. I.; Santiago, A.; He, M.; Asmar, F.; Weiner, B. R. Pressure and Temperature Dependence of the C_2H_3O + NO_2 Reaction. *Chem. Phys. Lett.* **1991**, *178*, 150−156.

(7) Liu, F.; Beames, J. M.; Petit, A. S.; McCoy, A. B.; Lester, M. I. Infrared-Driven Unimolecular Reaction of CH_3CHOO Criegee Intermediates to OH Radical Products. *Science* **2014**, *345*, 1596−1598.

(8) Osborn, D. L.; Choi, H.; Mordaunt, D. H.; Bise, R. T.; Neumark, D. M.; Rohlfing, C. M. Fast Beam Photodissociation Spectroscopy and Dynamics of the Vinoxy Radical. *J. Chem. Phys.* **1997**, *106*, 3049−3066.

(9) Morton, M. L.; Szpunar, D. E.; Butler, L. J. Photodissociating Methyl Vinyl Ether to Calibrate O + Ethylene Product Branching and to Test Propensity Rules for Product Channel Electronic Accessibility. *J. Chem. Phys.* **2001**, *115*, 204−216.

(10) Miller, J. L.; McCunn, L. R.; Krisch, M. J.; Butler, L. J.; Shu, J. Dissociation of the Ground State Vinoxy Radical and Its Photolytic Precursor Chloroacetaldehyde: Electronic Nonadiabaticity and the Suppression of the H + Ketene Channel. *J. Chem. Phys.* **2004**, *121*, 1830−1838.

(11) Matsika, S.; Yarkony, D. R. Photodissociation of the Vinoxy Radical Through Conical, and Avoided, Intersections. *J. Chem. Phys.* **2002**, *117*, 7198−7206.

(12) Piechowska-Strumik, K.; Lauvergnat, D.; Bacchus-Montabonel, M.-C.; Desouter-Lecomte, M. Quantum Dynamics Around a Non Planar Conical Intersection in Vinoxy Radical Relaxation. *Chem. Phys. Lett.* **2006**, *425*, 16−21.

(13) Young, R. A.; Yarkony, D. R. A Novel Conical Intersection Topography and Its Consequences: The 1, 2 ^2A Conical Intersection Seam of the Vinoxy Radical. *J. Chem. Phys.* **2005**, *123*, 084315.

(14) Bennett, D. I.; Butler, L. J.; Werner, H.-J. Comparing Electronic Structure Predictions for the Ground State Dissociation of Vinoxy Radicals. *J. Chem. Phys.* **2007**, *127*, 094309.

(15) McKown, B. G.; Ceriotti, M.; Womack, C. C.; Kamarchik, E.; Butler, L. J.; Bowman, J. M. Effects of High Angular Momentum on the Unimolecular Dissociation of CD_2CD_2OH: Theory and Comparisons with Experiment. *J. Phys. Chem. A* **2013**, *117*, 10951−10963.

(16) Brynteson, M. D.; Womack, C. C.; Booth, R. S.; Lee, S.−H.; Lin, J. J.; Butler, L. J. Radical Intermediates in the Addition of OH to Propene: Photolytic Precursors and Angular Momentum Effects. *J. Phys. Chem. A* **2014**, *118*, 3211−3229.

(17) The RRKM code is obtained from W. L. Hase and D. L. Bunker, *Quantum Chemistry Program Exchange 234*, 1974.

(18) Heck, A. J. R.; Chandler, D. W. Imaging Techniques for the Study of Chemical Reaction Dynamics. *Annu. Rev. Phys. Chem.* **1995**, *46*, 335−372.

(19) Eppink, A. T. J. B.; Parker, D. H. Velocity Map Imaging of Ions and Electrons Using Electrostatic Lenses: Application in Photoelectron and Photofragment Ion Imaging of Molecular Oxygen. *Rev. Sci. Instrum.* **1997**, *68*, 3477−3484.

(20) Chang, B.; Hoetzlein, R. C.; Mueller, J. A.; Geiser, J. D.; Houston, P. L. Improved Two-Dimensional Product Imaging: The Real-Time Ion Counting Method. *Rev. Sci. Instrum.* **1998**, *69*, 1665−1670.

(21) Dribinski, V.; Ossadtchi, A.; Mandelshtam, V. A.; Reisler, H. Reconstruction of Abel-Transformable Images: The Gaussian Basis-Set Expansion Abel Transform Method. *Rev. Sci. Instrum.* **2002**, *73*, 2634−2642.

(22) Curtiss, L. A.; Redfern, P. C.; Raghavachari, K.; Pople, J. A. Gaussian-3X (G3X) Theory: Use of Improved Geometries, Zero-Point Energies, and Hartree-Fock Basis Sets. *J. Chem. Phys.* **2001**, *114*, 108−117.

(23) Curtiss, L. A.; Redfern, P. C.; Raghavachari, K. Gaussian-4 Theory. *J. Chem. Phys.* **2007**, *126*, 084108.

(24) Frisch, M. J.; Trucks, G. W.; Schlegel, H. B.; Scuseria, G. E.; Robb, M. A.; Cheeseman, J. R.; Scalmani, G.; Barone, V.; Mennuci, B.; Petersson, G. A.; et al. *Gaussian09,* Revision A.02; Gaussian, Inc: Wallingford, CT, 2009.

(25) Liyanage, R.; Yang, Y.; Hashimoto, S.; Gordon, R. J.; Field, R. W. Electronic Control of the Spin-Orbit Branching Ratio in the Photodissociation and Predissociation of HCl. *J. Chem. Phys.* **1995**, *103*, 6811−6814.

(26) Adiabatic ionization energy calculated at the G4//B3LYP/6-311++G(3df,2p) level of theory.

(27) Savee, J. D.; Welz, O.; Taatjes, C. A.; Osborn, D. L. New Mechanistic Insights to the O(^{3}P) + Propene Reaction from Multiplexed Photoionization Mass Spectrometry. *Phys. Chem. Chem. Phys.* **2012**, *14*, 10410−10423.

(28) Lee, S.-H.; Huang, W.-J.; Chen, W.-K. Dynamics of the Reaction of Atomic Oxygen with Ethene: Observation of All Carbon-Containing Products by Single-Photon Ionization. *Chem. Phys. Lett.* **2007**, *446*, 276−280.

(29) NIST Chemistry WebBook http://webbook.nist.gov/chemistry/.

(30) Beyer, T.; Swinehart, D. F. Algorithm 448: Number of Multiply-Restricted Partitions. *Commun. ACM* **1973**, *16*, 379.

(31) Stein, S. E.; Rabinovitch, B. S. Accurate Evaluation of Internal Energy Level Sums and Densities Including Anharmonic Oscillators and Hindered Rotors. *J. Chem. Phys.* **1973**, *58*, 2438−2445.

(32) Brynteson, M. D.; Butler, L. J. Predicting the Effect of Angular Momentum on the Dissociation Dynamics of Highly Rotationally Excited Radical Intermediates. *J. Chem. Phys.* **2015**, *142*, 054301.

(33) Alligood, B. W.; Straus, D. B.; Butler, L. J. Analyzing Velocity Map Images to Distinguish the Primary Methyl Photofragments from those Produced upon C-Cl Bond Photofission in Chloroacetone at 193 nm. *J. Chem. Phys.* **2011**, *135*, 034302.

(34) Tabor, D. P.; Harding, M. E.; Ichino, T.; Stanton, J. F. High-Accuracy Extrapolated Ab Initio Thermochemistry of the Vinyl, Allyl, and Vinoxy Radials. *J. Phys. Chem. A* **2012**, *116*, 7668−7676.

(35) Townsend, D.; Lee, S. K.; Suits, A. G. DC Slice Imaging of CH_3Cl Photolysis at 193.3 nm. *J. Phys. Chem. A* **2004**, *108*, 8106−8114.

(36) Matsumi, Y.; Das, P. K.; Kawasaki, M. Doppler Spectroscopy of Chlorine Atoms Generated from Photodissociation of Hydrogen Chloride and Methyl Chloride at 157 and 193 nm. *J. Chem. Phys.* **1990**, *92*, 1696−1701.

(37) Matsumi, Y.; Das, P. K.; Kawasaki, M. Erratum: Doppler Spectroscopy of Chlorine Atoms Generated from Photodissociation of Hydrogen Chloride and Methyl Chloride at 157 and 193 nm [J. Chem. Phys. 92, 1696 (1990)]. *J. Chem. Phys.* **1992**, *97*, 5261.

(38) Lin, J. J.; Chen, Y.; Lee, Y. Y.; Lee, Y. T.; Yang, X. Photodissociation Dynamics of CH_3Cl at 157.6 nm: Evidence for $CH_2(\tilde{X}^3B_1/\tilde{a}^1A_1)$ + HCl Product Channels. *Chem. Phys. Lett.* **2002**, *361*, 374−382.